aerospace

MDPI

Article

Adjoint-Based Optimization of Overwing Nacelle and Wing Configuration

Chuang Yu [1], Ao Zhang [1], Fei Qin [1], Xian Chen [2] and Yisheng Gao [1,*]

[1] Aviation Academy, Nanjing University of Aeronautics and Astronautics, Nanjing 210016, China; yuchuang@nuaa.edu.cn (C.Y.); sx2301250@nuaa.edu.cn (A.Z.); qinfei_aero@nuaa.edu.cn (F.Q.)
[2] China Aerodynamics Research and Development Center, Mianyang 621013, China; climate_2007@yeah.net
* Correspondence: yishenggaogg@gmail.com

Abstract

A major development direction for next-generation civil aircraft is to significantly reduce fuel consumption through the integration of high-bypass-ratio engines. However, the large diameter of high BPR engines will cause traditional aircraft to face the dilemma of ground clearance. The over-the-wing engine mount configuration avoids ground clearance constraints by installing the engines over the wings, which is conducive to the integration of high BPR engines. However, the sensitivity of the flow on the upper surface of the wing makes this configuration more likely to cause strong interference between the engine and the wing than the traditional configuration. During the design, the important interaction of the wing shapes, the wing static elastic deformation, the engine installation position and the engine inlet and exhaust effect should be fully considered, which brings great challenges to the traditional design method. An automatic multidisciplinary coupled optimization method based on the discrete adjoint approach and gradient-based optimization is proposed for this configuration. A corresponding framework is established based on the open-source multidisciplinary optimization platform OpenMDAO; the CFD solution and the adjoint solution are carried out using the open-source CFD solver DAFoam; the structural finite element solution and the structural adjoint solution are carried out using the open-source FEM solver TACS; and the engine power effect is solved by coupling the intake and exhaust boundary conditions into the CFD solver. This method can comprehensively consider the changes in the wing shapes, the static aeroelastic deformation of the wing, the intake and exhaust effects of the engine, and the positional movement of the engine along the spanwise, chordwise and vertical directions of the wing. The optimization results show that the optimized configuration eliminates the strong shock interaction between the nacelle and the wing, enhances the favorable pressure gradient on the upper surface of the wing, and reduces the drag by 9.51%, thereby demonstrating the effectiveness of the proposed multidisciplinary coupled adjoint optimization method for this configuration.

Keywords: over-the-wing engine mount; multidisciplinary coupling; adjoint method; static aeroelasticity; interference resistance

Received: 24 February 2026
Revised: 2 April 2026
Accepted: 7 April 2026
Published: 8 April 2026

1. Introduction

The development of conventional civil aircraft configurations has gradually reached a plateau in terms of fuel efficiency improvement, and the potential for further enhancement through incremental modifications of traditional layouts is becoming increasingly limited.

One of the most important development directions for next-generation civil aircraft is to significantly reduce fuel consumption by increasing the engine bypass ratio to approximately 12–20 [1]. However, the continuous increase in bypass ratio inevitably leads to a substantial growth in engine diameter, which causes conventional under-wing engine installations to face severe ground clearance constraints.

The over-the-wing engine mount configuration relocates the engines from beneath the wing to above the main wing, fundamentally avoiding ground clearance limitations. This configuration facilitates the integration of large or ultra-high bypass ratio engines and allows for convenient future engine upgrades, thereby offering a promising solution for improving fuel efficiency. In addition, the shielding effect provided by the main wing can significantly reduce takeoff and landing noise, while the reduced landing gear height contributes to a lower overall structural weight of the landing system. Moreover, compared with traditional layouts, this configuration requires relatively modest architectural changes and can retain many proven design advantages, thereby reducing technical and operational risks. A conceptual illustration of the over-the-wing engine mount configuration is shown in Figure 1.

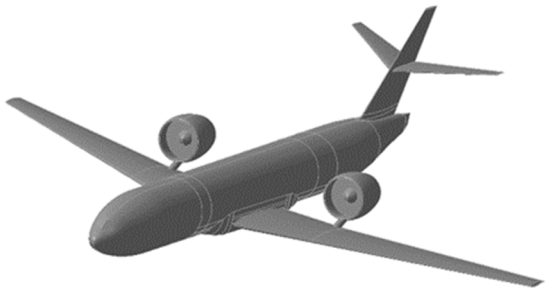

Figure 1. Conceptual illustration of the over-the-wing engine mount.

Despite these advantages, the over-the-wing engine mount configuration introduces additional technical challenges when compared with conventional layouts. From an aerodynamic perspective, the engine installation position, pylon configuration, and engine inlet and exhaust effects can significantly alter the flow field over the wing. Improper engine placement is more likely to induce strong aerodynamic interference between the wing and the engine, while the inlet suction effect of the engine fan can generate localized high-pressure regions on the upper surface of the wing, thereby affecting lift performance. Furthermore, with the increasing application of composite materials in future civil aircraft, aeroelastic deformation of the wing during flight has become more pronounced. As a result, during the design and optimization of over-the-wing engine configurations, the interactions among wing geometry, static aeroelastic deformation, engine installation position, and engine inlet and exhaust effects must be fully considered.

Traditional aircraft design approaches typically adopt a sequential strategy in which the airframe and engine are designed separately and subsequently integrated. For over-the-wing engine mount configurations, such a strategy is prone to introducing excessive interference drag and suboptimal aerodynamic performance. Consequently, there is a strong need for a fully automated optimization methodology capable of handling the tightly coupled interactions among aerodynamic, structural, and propulsion disciplines. Applying such a method to the design process of over-the-wing engine configurations is essential for identifying integrated design solutions that can fully exploit the advantages of this layout.

Several studies have investigated optimization strategies for over-the-wing engine configurations. Berguin and Mavris [2] conducted an optimization study based on sensitivity analysis and adjoint methods without considering engine inlet and exhaust effects, and

demonstrated that integrated optimization can significantly reduce cruise interference drag for this type of configuration. Abdul-Kaiyoom et al. [3] performed an aeropropulsive coupled adjoint optimization for an over-the-wing engine configuration while simultaneously optimizing the wing shape and engine cross-sectional geometry; however, pylon effects and engine positional variations were not included in their study. Lange et al. [4] applied a fully automated surrogate-based optimization method to an aircraft equipped with an ultra-high bypass ratio engine, optimizing the engine position in both horizontal and vertical directions. Their results showed that cruise drag could be reduced by approximately 11% through engine position optimization alone. Fujino and Kawamura [5] systematically investigated the wave-drag characteristics of an over-the-wing nacelle configuration and showed that wave-drag reduction can be achieved when the nacelle front face is located near the shock position on the wing, with the vertical spacing maintained in an appropriate range. More recently, Ahuja et al. [6] analyzed the sensitivity of drag, lift, and pressure recovery to engine installation location and engine operating condition, and further showed that outer-mold-line contouring is as critical as nacelle translation; therefore, nacelle placement studies in isolation are insufficient for aerodynamically competitive OWN concepts.

From an engineering application perspective, the successful development of the HondaJet by Honda Aircraft Company (Greensboro, NC, USA) [7] further demonstrates the feasibility and practical value of the over-the-wing engine mount configuration.

Adjoint-based multidisciplinary design optimization (MDO) methods have proven to be highly efficient for aircraft configuration optimization problems involving strong coupling and large design spaces. The University of Michigan MDO Laboratory developed an aerostructural adjoint framework based on the Navier–Stokes solver ADflow (Burlington, ON, Canada) [8] and the structural finite element solver TACS [9], which was subsequently integrated into the high-fidelity MACH-Aero optimization platform [10]. NASA (Washington, DC, USA) developed the OpenMDAO framework [11] based on unified derivative theory to enable efficient solution of coupled multiphysics systems using Newton-type algorithms, and to support applications such as aerostructural and aeropropulsive coupling. Building upon OpenMDAO, He et al. developed the DAFoam solver [12] with discrete adjoint capabilities based on OpenFOAM [13], and coupled it with the open-source structural solver TACS to perform aerostructural adjoint optimization. In addition, Hendricks et al. developed the open-source engine cycle analysis code pyCycle v4.4.0 [14], which incorporates adjoint gradient computation capabilities to address limitations of the Numerical Propulsion System Simulation (NPSS) platform [15]. This tool has been successfully integrated into adjoint-based aeropropulsive optimization frameworks, such as those developed by the University of Michigan MDO Laboratory (Ann Arbor, MI, USA) [16].

These previous studies indicate that the favorable interference of over-the-wing engine configurations depends on the matching between nacelle placement and the wing shock system, while aerodynamically competitive designs require coordinated consideration of nacelle placement and airframe outer-mold-line shaping.

While previous studies have explored over-the-wing engine configurations or MDO frameworks independently, the originality of the present study lies in the high-fidelity aerostructural coupling specifically tailored for this unique configuration using a fully open-source framework. Furthermore, it uniquely investigates the coupled mechanisms of static aeroelastic deformation and nacelle repositioning on the upper-wing shock structures.

Motivated by these advances, the present study investigates a comprehensive multidisciplinary coupled optimization methodology for over-the-wing engine mount configurations based on unstructured-grid discrete adjoint methods. The proposed approach focuses on the development of coupled derivative computation and adjoint optimization techniques involving aerodynamic, structural, and propulsion disciplines, as well as the

associated shape parameterization methods, relative motion parameterization for multiple components, and dynamic mesh deformation techniques. Based on these developments, a complete multidisciplinary coupled analysis and discrete adjoint-based drag reduction optimization framework for over-the-wing engine configurations is established using the open-source OpenMDAO platform. This framework enables the simultaneous consideration of wing airfoil shape variations and twist, static aeroelastic deformation, engine inlet and exhaust effects, and engine positional movements in the spanwise, chordwise, and vertical directions. The framework is subsequently applied to cruise drag reduction optimization of an over-the-wing engine configuration, and the results demonstrate its effectiveness while providing insights into design strategies for reducing interference drag and maintaining lift performance.

2. Computational Method

2.1. Flow Solver

The flow field is solved using DARhoSimpleCFoam, which is integrated in the open-source aerodynamic adjoint optimization framework DAFoam. This solver evaluates the compressible Navier–Stokes equations using a compressible form of the SIMPLEC algorithm [17]. The system is closed using the Spalart–Allmaras one-equation turbulence model [18].

2.2. Structural Finite Element Solver

For the structural discipline, the open-source solver TACS is employed for structural finite element analysis and subsequent gradient/adjoint computations. In TACS, the structure is modeled using shell elements, and the global equilibrium equations are solved using a domain-decomposition-based parallel direct matrix factorization method. The governing equation of linear elasticity can be written in the standard form.

2.3. Aerostructural Coupling Method

The aerodynamic mesh and the structural mesh are two independent discretizations, solved separately by computational fluid dynamics (CFD) and the finite element method (FEM), respectively. Therefore, a load–displacement transfer strategy is required to establish the coupling between the aerodynamic and structural problems. Specifically, the displacement induced by structural surface deformation must be transferred to the aerodynamic surface mesh, and the aerodynamic loads acting on the aerodynamic surface mesh must be transferred back to the structural surface mesh.

In this study, the rigid link transfer method developed by Kennedy and Martins [19] is adopted. A tightly coupled aerostructural solution strategy is employed. Compared with a loosely coupled approach, the tightly coupled method exchanges data between disciplines before each single-discipline solution is fully converged (i.e., after partial convergence), which enables both improved accuracy and computational efficiency.

By assembling the aerodynamic and structural governing equations in residual form within a global coordinate system, the coupled residual system can be expressed as Equation (1).

$$\boldsymbol{R} = \begin{bmatrix} \boldsymbol{R}_{CFD}(\boldsymbol{w}_{FEM}, \boldsymbol{w}_{CFD}) \\ \boldsymbol{R}_{FEM}(\boldsymbol{w}_{FEM}, \boldsymbol{w}_{CFD}) \end{bmatrix} = 0 \tag{1}$$

Here, $\boldsymbol{R}_{CFD}$ denotes the residual of the aerodynamic governing equations, and $\boldsymbol{R}_{FEM}$ denotes the residual of the structural governing equations. The corresponding state variables are $\boldsymbol{w}_{FEM}$ and $\boldsymbol{w}_{CFD}$, which represent the structural displacement state and the flow field state, respectively. The tightly coupled aerostructural solution in this work is implemented using the aerostructural scenario provided by the OpenMDAO multiphysics library

MPhys [20], and the load and displacement transfer is performed through the FUNtoFEM utilities integrated within MPhys.

The overall workflow of the tightly coupled aerostructural analysis is illustrated in Figure 2. Schematic of the tightly coupled aerostructural solution procedure. The black nodes denote structural states, the arrows indicate discipline solution or load/displacement transfer directions, and the red circled numbers indicate the execution sequence within one coupling cycle.

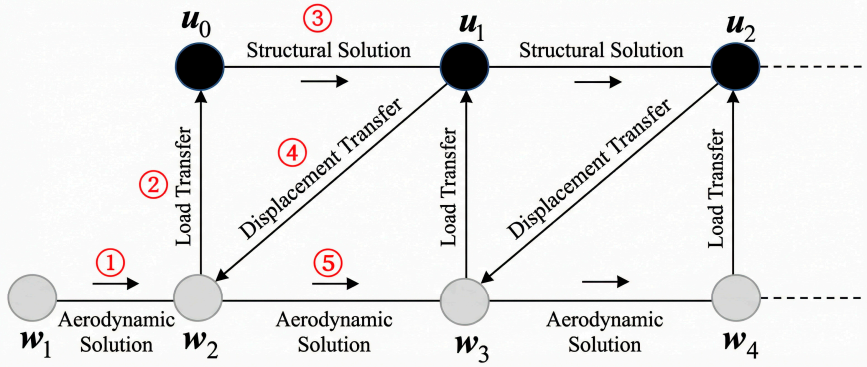

Figure 2. The diagram for aerostructural coupling.

2.4. Modeling of Engine Jet/Power Effects

In this study, the engine jet/power effects are simplified and modeled using a zero-dimensional approach by prescribing inlet and exhaust boundary conditions in the CFD solver. Based on characteristic line theory [21], the boundary-condition treatment is illustrated in Figure 3. The engine inlet is located at the fan station and is treated as a subsonic outflow boundary, where the static pressure is specified.

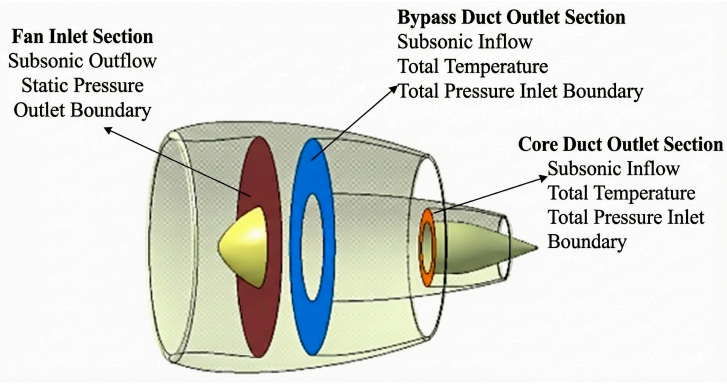

Figure 3. The boundary conditions of engine simulation.

The engine exhaust consists of two outlets, corresponding to the bypass nozzle and the core nozzle. At these two exit planes, total temperature and total pressure are prescribed as boundary conditions. The static pressure is obtained by extrapolation/interpolation from the internal flow field. Using the thermodynamic relations between total and static quantities, the Mach number at the outlet boundary can be determined, and other flow properties at the outlet boundary can then be computed accordingly.

It should be noted that this boundary condition treatment primarily captures the jet-induced aerodynamic interference effects on the external flow field. It does not account for the feedback of external aerodynamic or structural states on the engine's internal thrust performance.

2.5. Aerostructural Coupled Adjoint Method

Based on the fundamental principles of adjoint equations, the aerostructural coupled adjoint problem is formulated using a block Gauss–Seidel strategy, yielding the aerostructural coupled adjoint system (Equation (2)). The aerodynamic adjoint equations are solved using DAFoam (Equation (3)).

$$\begin{bmatrix} \frac{\partial \boldsymbol{R}_{CFD}}{\partial \boldsymbol{w}_{CFD}}^T & \frac{\partial \boldsymbol{R}_{FEM}}{\partial \boldsymbol{w}_{CFD}}^T \\ \frac{\partial \boldsymbol{R}_{CFD}}{\partial \boldsymbol{w}_{FEM}}^T & \frac{\partial \boldsymbol{R}_{FEM}}{\partial \boldsymbol{w}_{FEM}}^T \end{bmatrix} \begin{bmatrix} \boldsymbol{\psi}_{CFD} \\ \boldsymbol{\psi}_{FEM} \end{bmatrix} = \begin{bmatrix} \frac{\partial f}{\partial \boldsymbol{w}_{CFD}}^T \\ \frac{\partial f}{\partial \boldsymbol{w}_{FEM}}^T \end{bmatrix} \tag{2}$$

$$\frac{\partial \boldsymbol{R}_{CFD}}{\partial \boldsymbol{w}_{CFD}}^T \boldsymbol{\psi}_{CFD} = \frac{\partial f}{\partial \boldsymbol{w}_{CFD}}^T \tag{3}$$

A Jacobian-free adjoint matrix technique is adopted for the adjoint solution [22]. Automatic differentiation is used to compute partial derivatives and Jacobian–vector products. The coupled linear system is solved using the generalized minimal residual method (GMRES). A multilevel technique is used for global preconditioning, and an incomplete LU (ILU) factorization is employed for local preconditioning.

$$\frac{\partial \boldsymbol{R}_{FEM}}{\partial \boldsymbol{w}_{FEM}}^T \boldsymbol{\psi}_{FEM} = \frac{\partial f}{\partial \boldsymbol{w}_{FEM}}^T \tag{4}$$

For the structural discipline, TACS is used to solve the structural adjoint equations (Equation (4)). The aerodynamic–structural coupling is reflected by the off-diagonal cross-derivative terms in Equation (2).

In this work, the aerostructural coupled adjoint system is solved using the Modular Analysis and Unified Derivatives (MAUD) methodology as implemented within the OpenMDAO–MPhys framework. Compared with conventional coupled adjoint methods, which often require deriving and implementing problem-specific coupled adjoint formulations depending on the solution procedures of each discipline (thereby limiting extensibility), the MAUD approach collects all inputs, states, and outputs of each discipline into a unified vector and represents the multidisciplinary model as a single implicit nonlinear system. The system is then linearized in a unified manner, enabling consistent derivative treatment across disciplines. Under MAUD, the user only needs to provide the partial derivatives for each discipline model, after which total derivatives and coupling derivatives among disciplines can be computed automatically, substantially reducing the implementation burden of multidisciplinary coupled adjoint methods.

The formulation and solution of the aerostructural multidisciplinary coupled adjoint system are implemented using NASA's open-source multidisciplinary optimization framework OpenMDAO. In multidisciplinary coupled adjoint computations, large amounts of data must be exchanged among discipline components, and the coupled solution must follow a prescribed execution order. OpenMDAO is a general framework centered on MAUD for modular analysis and unified derivative computation. For multidisciplinary coupling problems, the multiphysics library MPhys built on OpenMDAO provides standard discipline interfaces. Users implement discipline-specific analysis and derivative computation modules, assemble the disciplines into a hierarchical model via MPhys, and define interconnections among disciplines. The coupled adjoint equations are then solved within OpenMDAO to obtain total derivatives. The matrix data connectivity of the aerostructural coupled solution constructed in this work based on the OpenMDAO multiphysics library MPhys is illustrated in Figure 4.

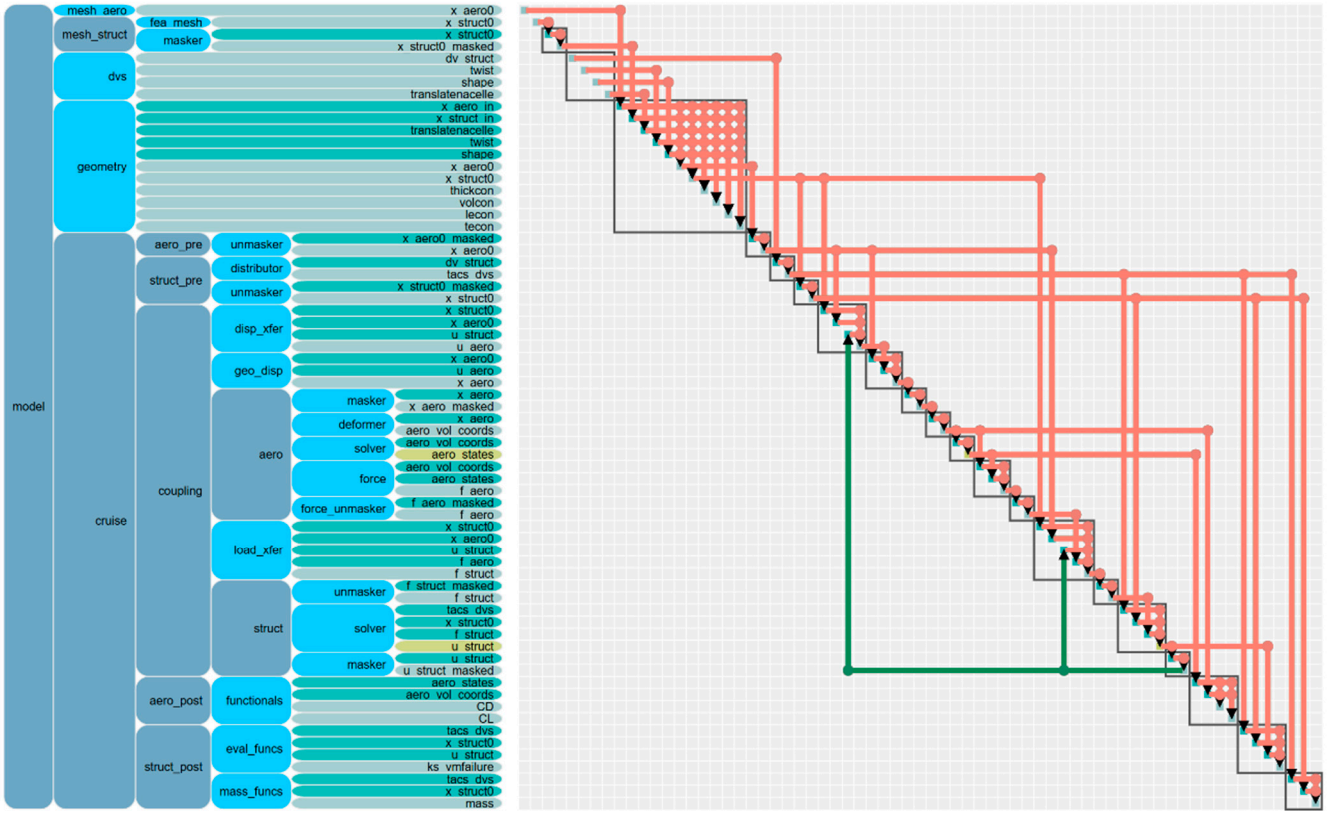

Figure 4. The coupling matrix of aerostructural scenario in OpenMDAO.

Figure 4: Coupling matrix of the aerostructural scenario in OpenMDAO. Different colors indicate different types of model blocks/data couplings, and the black triangles denote nonzero entries in the assembled coupling matrix.

Software information: The software used in this study included DAFoam v3.1.3, TACS v3.10.0, and pyGeo v1.17.0. The aerostructural coupled implementation was carried out within the OpenMDAO–MPhys framework v2.0.0, and mesh deformation was handled using IDWarp v2.6.4. The aerodynamic mesh and structural finite-element mesh were generated using ICEM CFD 2026 and MSC Nastran 025.1, respectively.

3. Case Setup

Prior to the optimization process, a multidisciplinary coupled analysis of the initial configuration is required in order to obtain the baseline flow field, aerodynamic performance, and structural deformation. All subsequent optimization iterations are conducted based on this converged baseline solution. In the following, the case setup is described in terms of mesh generation, operating conditions, multidisciplinary coupled analysis, and result assessment.

3.1. Mesh Description of the Initial Configuration

Multidisciplinary coupled analysis requires two independent discretizations: an aerodynamic mesh and a structural mesh. The aerodynamic mesh is generated using ICEM CFD and consists of a conventional unstructured hybrid grid. Triangular elements are used on the surface, tetrahedral elements are employed in the far-field volume, and prismatic elements are adopted for the boundary-layer region.

To accurately capture geometric curvature and flow features in critical regions, anisotropic meshes are generated at the wing leading edge, engine lip, bypass duct, and core duct exit using the Autoblock method. The transonic compressible solver DARhoSim-

pleCFoam is used for aerodynamic analysis. In this solver, turbulence is modeled using wall functions, and a recommended wall-normal resolution of y+ ≈ 30 is adopted. Accordingly, the first-layer thickness of the boundary-layer mesh is set to 0.14 mm, with a total of 24 layers and a growth ratio of 1.25. The total number of aerodynamic mesh cells is approximately 2.2 million.

The wing structural model is represented in the form of a wingbox, which serves as the primary load-bearing structure of the wing. The wingbox consists of front and rear spars, internal ribs, upper and lower skins, and longitudinal stringers. The wingbox geometry is connected to the center wingbox near the wing root. A total of 21 ribs are distributed along the spanwise direction, aligned with the freestream, and 9 longitudinal stringers are arranged in the chordwise direction on both the upper and lower skins.

The structural finite element mesh is generated using MSC Nastran. All wingbox components are modeled using two-dimensional shell elements, and quadrilateral elements are adopted throughout the mesh. The structural mesh consists of 7346 nodes and 7632 elements. The aerodynamic and structural meshes are strictly defined in the same global coordinate system, and their surface correspondence is ensured to enable accurate load and displacement transfer. The relationship between the aerodynamic and structural meshes is illustrated in Figure 5.

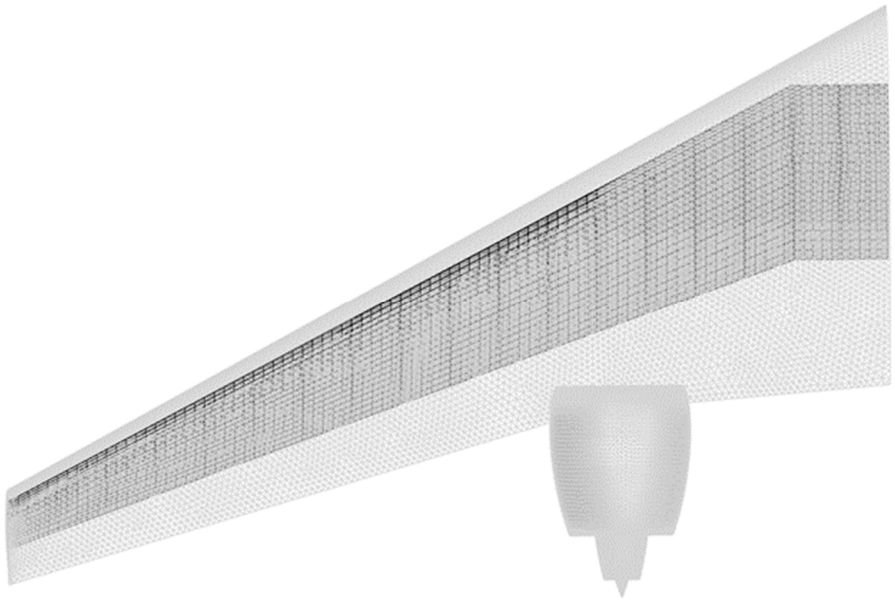

Figure 5. The relation of aerodynamic and structural mesh.

3.2. Multidisciplinary Coupled Analysis of the Initial Configuration

The present study focuses on drag reduction optimization of an over-the-wing engine configuration under cruise conditions. Therefore, the initial multidisciplinary coupled analysis corresponds to a cruise flight scenario. The design cruise conditions are specified as follows: flight altitude of 9 km, cruise Mach number Ma = 0.77, angle of attack AOA = 2.75°, and Reynolds number Re = 2.647×10^7. During cruise, the engine inlet and exhaust conditions are assumed to remain constant, and the mass flow ratio between the bypass and core exhaust is set to 14.

The freestream flow conditions used in the aerodynamic simulation are summarized in Table 1.

The engine inlet and exhaust boundary conditions are listed in Table 2. These boundary conditions are defined with reference to the over-the-wing engine configuration CRC 880 REF3 developed by the German Aerospace Center [23], which is equipped with a high-

bypass-ratio engine. The prescribed inlet and exhaust conditions were verified through preliminary flow field tests. After convergence, the mass flow rate at the fan inlet is 240 kg/s, while the mass flow rates at the bypass and core exhaust outlets are 224 kg/s and 16 kg/s, respectively, yielding a bypass-to-core mass flow ratio of 14, which is consistent with the flow characteristics of high-bypass-ratio engines.

Table 1. Flow field state parameters.

Parameter	Value
Freestream static pressure/Pa	30,801
Freestream static temperature/K	230
Freestream density/kg/m^3	0.467
Freestream Mach number	0.77
Freestream angle of attack/°	2.75
Freestream dynamic viscosity/N·s/m^3	1.4926×10^{-5}

Table 2. Engine inlet and exhaust boundary parameters.

Parameter	Value
Fan exit static pressure/Pa	36,405
Bypass duct inlet total pressure/Pa	65,084
Bypass duct inlet total temperature/K	271
Core duct inlet total pressure/Pa	57,692
Core duct inlet total temperature/K	586

For the structural analysis, the wingbox is assumed to be made of 7075 aluminum alloy. To simplify the coupled optimization system, a smeared stiffness approach [24] is adopted, and the thickness of all structural components is uniformly set to 3 mm. The material properties of the wingbox are summarized in Table 3.

Table 3. Material properties of the wingbox.

Parameter	Value
Density/kg·m^{-3}	2780
Young's modulus/Pa	73.1×10^9
Poisson's ratio	0.33
Shear correction factor	5/6
Yield strength/Pa	324×10^6

It should be further noted that the present structural model only includes the wingbox shell structure, and the aerostructural coupling accounts for the cruise static aeroelastic deformation induced by aerodynamic load transfer. The engine is not explicitly modeled as a structural component in the present study; instead, its propulsion effect is represented through prescribed inlet and exhaust boundary conditions in the CFD solver. Therefore, engine concentrated mass, pylon structural stiffness, gravity/inertial loads, and the additional structural load redistribution associated with engine-position changes are not included in the present structural model. Accordingly, the present structural results should be interpreted as cruise-point static aeroelastic responses of a simplified wingbox model, rather than as a complete structural or flutter-feasibility assessment of the engine–pylon–wing system.

Before conducting the coupled analysis, a grid convergence study is performed using three aerodynamic meshes: a coarse mesh (1.0 million cells), a medium mesh (2.2 million

cells), and a fine mesh (4.0 million cells). The converged results for these meshes are compared in Table 4.

Table 4. Grid convergence study for different mesh resolutions.

Mesh Level	C_L	C_D	Relative Error of C_L (%)	Relative Error of C_D (%)
Coarse mesh	0.4476	0.04935	−0.096	−2.859
Medium mesh	0.4461	0.05035	−0.042	−0.881
Fine mesh	0.4479	0.05079	0	0

The results indicate that the differences in lift and drag coefficients between the medium and fine meshes are both within 1%. Therefore, in order to reduce the computational cost of the subsequent coupled adjoint optimization, the medium mesh with 2.2 million cells is selected for the remainder of this study.

The initial multidisciplinary coupled analysis is performed using the flow solver DARhoSimpleCFoam and the structural solver TACS. In the tightly coupled aerostructural solution, a convergence tolerance must be specified. Once this tolerance is reached, the aerodynamic solution is considered sufficiently converged to allow load transfer to the structural solver. A smaller tolerance improves solution accuracy but significantly increases the overall computational cost, particularly for subsequent adjoint-based optimization. Therefore, an appropriate tolerance must be selected to balance accuracy and efficiency.

To this end, a convergence study is conducted using four different tolerances: 1×10^{-4}, 1×10^{-5}, 1×10^{-6}, and 1×10^{-7}. The converged aerodynamic results are compared in Table 5.

Table 5. Convergence comparison under different residual tolerances.

Allowable	1×10^{-4}	1×10^{-5}	1×10^{-6}	1×10^{-7}
C_L	0.37059	0.37024	0.37043	0.37017
C_D	0.045684	0.045537	0.045537	0.045534

The results show that a tolerance of 1×10^{-4} leads to noticeable accuracy degradation, whereas the results obtained with tolerances of 1×10^{-5} and 1×10^{-6} differ from those obtained with 1×10^{-7} by less than 0.07024% in lift coefficient and 0.00659% in drag coefficient. Therefore, a tolerance of 1×10^{-5} is selected for both the initial coupled analysis and the subsequent coupled adjoint optimization.

The maximum number of flow solver iterations per coupling cycle is set to 1000. After 24 coupling cycles, the multidisciplinary coupled analysis converges to the specified tolerance. The resulting aerodynamic coefficients are summarized in Table 6, while the convergence histories of the flow solver and aerodynamic forces are shown in Figures 6 and 7, respectively.

Table 6. Aerodynamic results of the initial aerostructural solution.

	Converged Results of the Initial Configuration	Converged Results of the Initial Aerostructural Solution
C_L	0.4461	0.3702
C_D	0.05035	0.04559

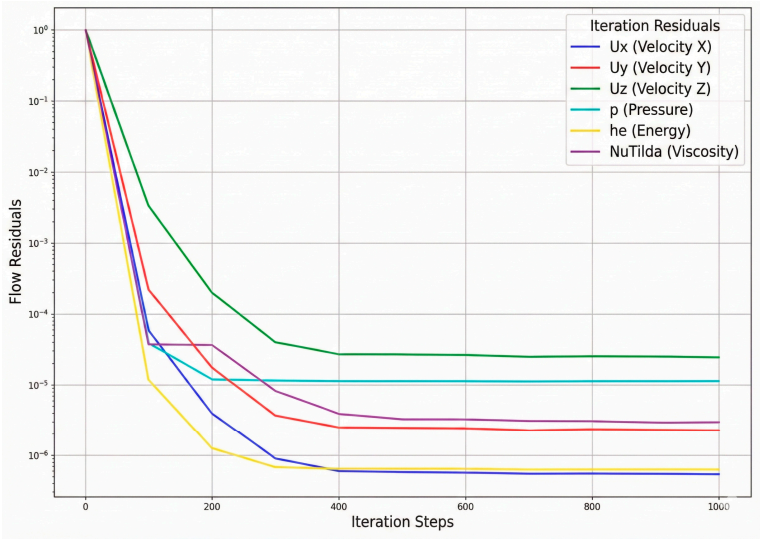

Figure 6. Convergence history of the flow field solution during aerostructural coupling.

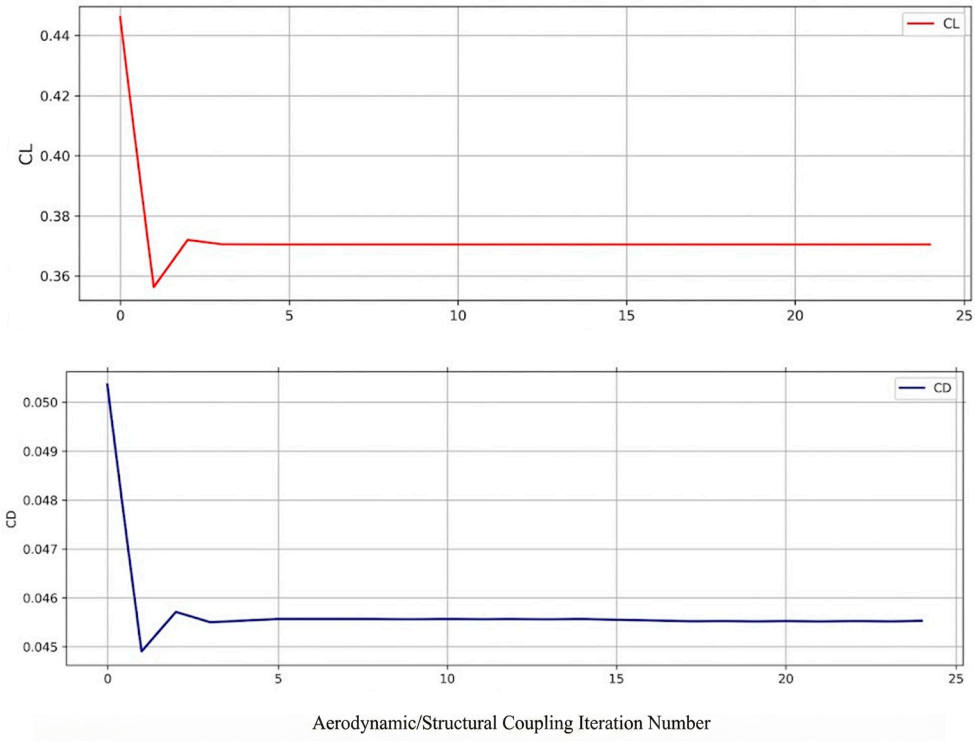

Figure 7. Convergence history of aerodynamic forces during aerostructural coupling.

It should be noted that the "initial configuration converged results" correspond to the converged solution obtained without considering static aeroelastic deformation, whereas the "initial aerostructural converged results" represent the converged solution obtained from the fully coupled aerostructural analysis.

The changes in the wing geometry during the coupled analysis is illustrated in Figure 8, where the gray surface represents the initial configuration and the green surface corresponds to the converged aeroelastically deformed shape. The aerostructural coupling process is inherently dynamic. In the early stages, the aerodynamic loads are relatively large due to incomplete convergence, resulting in significant structural deformation. As the solution progresses, the aerodynamic loads gradually converge, and the structural deformation approaches the final aeroelastic equilibrium shape.

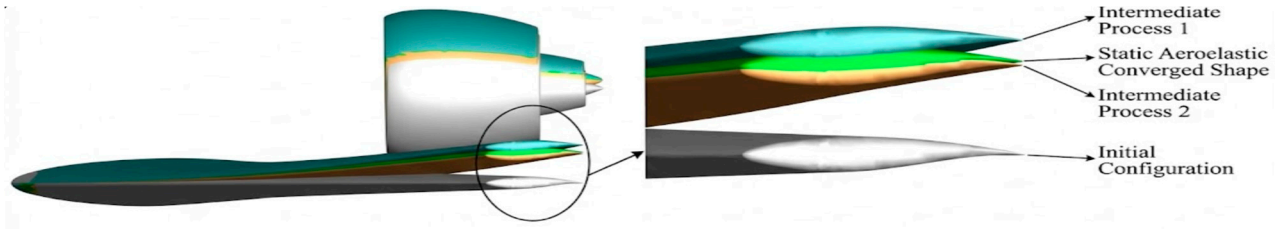

Figure 8. The shape changes in aerostructural solution.

A comparison of aerodynamic forces indicates that static aeroelastic effects have a substantial impact on aerodynamic performance. Compared with the converged solution of the undeformed initial configuration, the lift coefficient C_L decreases by 17.01%, and the drag coefficient C_D decreases by 9.55% after aeroelastic deformation is considered. This behavior can be attributed to the positive bending deformation and negative sectional twist induced by wing structural elasticity in swept wings. The negative twist reduces the effective local angle of attack, leading to a reduction in aerodynamic forces.

Figure 9 presents a comparison of wing sectional displacement and twist before and after aeroelastic deformation along the spanwise direction. Near the wing root, the differences are negligible; however, from the mid-span toward the wing tip, both displacement and twist differences increase progressively.

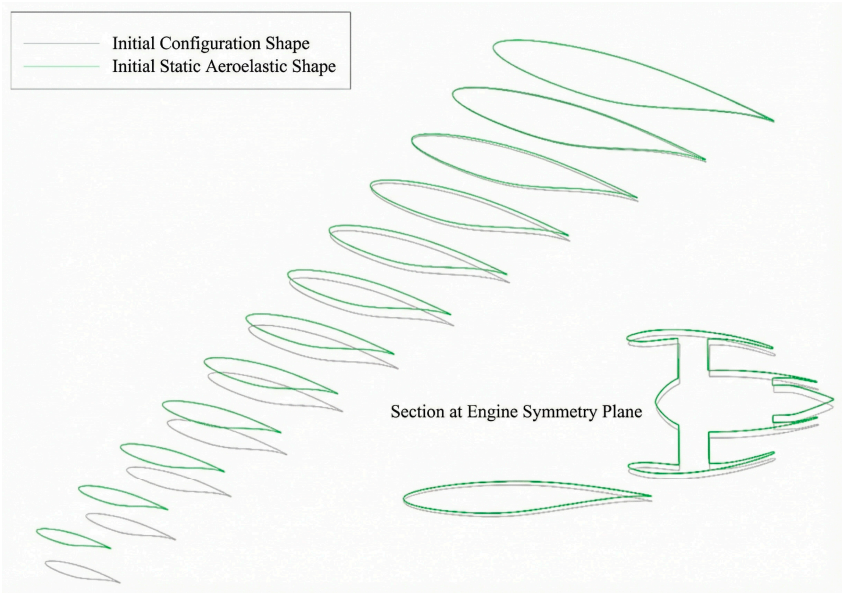

Figure 9. Comparison of airfoil profile after aerostructural solution.

To further illustrate the change in sectional twist, six spanwise sections are selected along the half-span from root to tip. For each section, the airfoil shapes before and after aeroelastic deformation are superimposed at the same reference origin to eliminate translational effects. The comparison is shown in Figure 10, where the percentages indicate the spanwise locations along the half-span. The results clearly demonstrate that all sections experience negative twist after aeroelastic deformation, with the magnitude increasing toward the wing tip.

Flow field visualization at the engine symmetry plane reveals a pronounced influence of the engine jet on the external flow. In particular, a high-pressure region forms on the upper surface of the wing upstream of the fan inlet, reducing the local flow velocity compared with a clean wing configuration. This effect decreases the pressure difference between the upper and lower wing surfaces and weakens lift. Moreover, comparison of

pressure coefficient distributions before and after aeroelastic deformation shows that strong shock waves persist near the nacelle leading edge and at the interaction region between the nacelle and the wing trailing edge. These shock structures are identified as the primary source of interference drag for over-the-wing engine configurations. The comparison is shown in Figure 11.

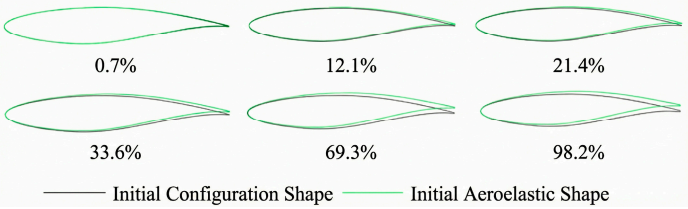

Figure 10. Comparison of airfoil twist angle after aerostructural solution.

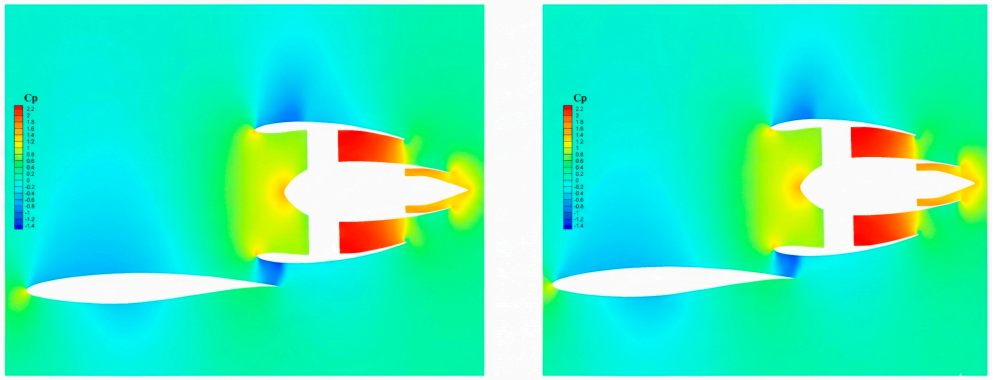

Figure 11. Comparison of pressure coefficient distributions at the engine symmetry plane before and after aeroelastic deformation.

3.3. Multidisciplinary Coupled Adjoint Optimization

The optimization scenario considered in this study focuses on cruise drag reduction for an over-the-wing engine configuration. Based on the multidisciplinary coupled analysis and discrete adjoint optimization framework developed in this work, the optimization simultaneously accounts for wing shape variations, static aeroelastic deformation, engine jet effects, and engine positional movements in the spanwise, chordwise, and vertical directions. The objective of the optimization is to minimize the drag coefficient at the cruise condition while satisfying the prescribed lift lower bound.

The flow field conditions and engine inlet and exhaust states during the optimization are identical to those used in the initial aerostructural analysis described in Section 3.2. The converged result of the initial aerostructural solution serves as the baseline (iteration 0) for the optimization. During the optimization process, the angle of attack is fixed at 2.75°, and the engine inlet and exhaust conditions remain unchanged. As the wing shape and engine position evolve, the aerodynamic loads are dynamically updated and interact with the structural displacements to continuously update the aeroelastically deformed configuration until convergence of the optimization is achieved.

The geometric parameterization required for optimization is implemented using a multi-block pyGeo free-form deformation (FFD) [25] approach. Two FFD blocks are constructed, as illustrated in Figure 12. The primary FFD block (highlighted by the red box) encloses the main wing. This block contains 30 spanwise wing sections, and each section is controlled by 15 control points on both the upper and lower surfaces, resulting in a total of 450 FFD control points. Vertical displacements of these control points are used to modify

the airfoil shapes and thus control the wing geometry. In addition, the wing sections can be rotated about a predefined twist reference axis to control the sectional twist distribution.

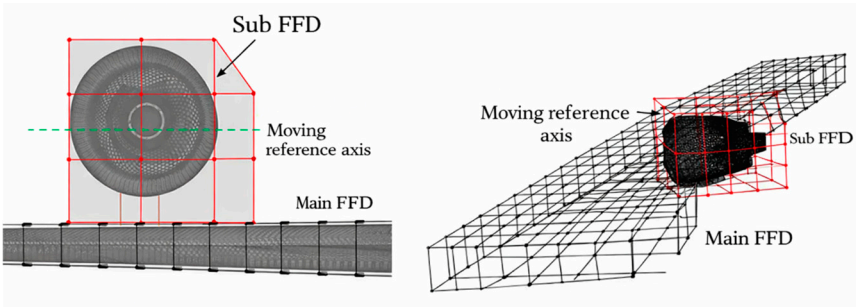

Figure 12. Multi-block FFD control framework.

The secondary FFD block (highlighted by the blue box) encloses the engine nacelle. This block controls the engine motion by translating the nacelle along a reference axis located near the nacelle leading edge, enabling engine positional movements in the spanwise, chordwise, and vertical directions. The effects of the multi-block FFD parameterization are illustrated in Figures 12 and 13. The geometry deformations induced by parameterized shape updates and static aeroelastic deformation are handled using the dynamic mesh deformation method provided by the IDWarp module [26].

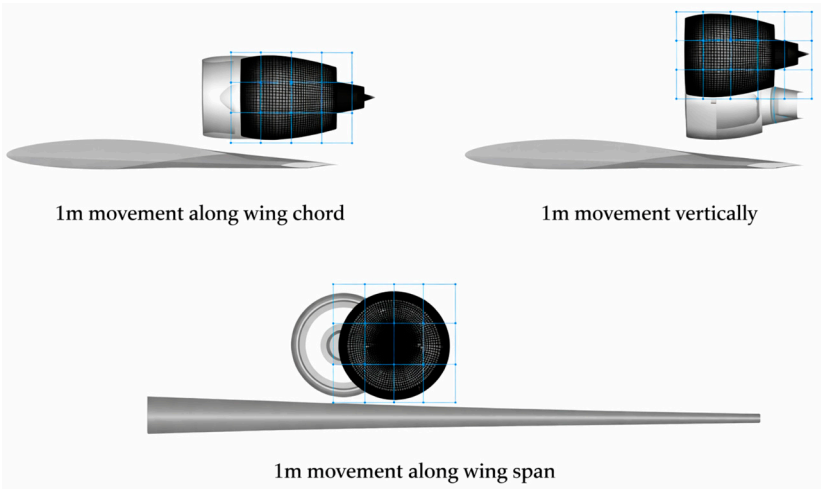

Figure 13. Illustration of engine movements in three directions relative to the wing.

Figure 12: Multi-block FFD control framework. The black wireframe denotes the main-wing FFD block, the red wireframe denotes the nacelle sub-FFD block, and the dashed line indicates the reference axis for nacelle translation.

The optimization problem is defined by the objective function, design variables, and constraints, as summarized in Table 7. The ranges of the design variables and the constraint definitions are carefully selected to ensure both numerical robustness of the optimization process and engineering feasibility of the optimized design.

The optimization objective is to minimize the drag coefficient C_D at the cruise condition. The design variables include:

Vertical displacements of the 450 wing FFD control points, within the range of -0.015 m to $+0.015$ m, to control wing shape deformation;

Sectional twist angles of the 30 wing sections, with a maximum allowable twist variation of $\pm 2^\circ$;

Table 7. Optimization settings.

Category	Variable/Function	Description	Number	Total
Design variables	$-0.015\ \text{m} \leq \text{Y} \leq 0.015\ \text{m}$	Vertical displacement of main FFD control points for wing shape deformation	450	
	$-2^\circ \leq \gamma \leq 2^\circ$	Sectional airfoil twist angles for wing twist control	30	
	$-1\ \text{m} \leq \text{X} \leq 1\ \text{m}$	Engine chordwise translation controlled by sub-FFD	1	
	$-0.3\ \text{m} \leq \text{Y} \leq 1\ \text{m}$	Engine vertical translation controlled by sub-FFD	1	
	$-1\ \text{m} \leq \text{Z} \leq 1\ \text{m}$	Engine spanwise translation controlled by sub-FFD	1	483
Constraints	$\text{C}_\text{L} = 0.3702$	Lift coefficient constraint at the cruise condition	1	
	$\text{V} \geq \text{V}_\text{initial}$	Wing volume constraint	1	
	$0.5\ \text{T}_\text{initial} \leq \text{T} \leq 3\ \text{T}_\text{initial}$	Airfoil thickness constraint at each wing section	450	
	$\triangle\text{Y}_\text{LEup} = \triangle\text{Y}_\text{LEdown}$	Leading-edge shape constraint	30	
	$\triangle\text{Y}_\text{TEup} = \triangle\text{Y}_\text{TEdown}$	Trailing-edge shape constraint	30	
	$\text{VM}_\text{stress} \leq 0.64$	Material failure constraint (safety factor of 1.5)	1	513

Translational motions of the engine FFD block in the chordwise, vertical, and spanwise directions.

The constraints imposed in the optimization include:

A lower-bound constraint on the lift coefficient, $\text{C}_\text{L} = 0.3702$, to ensure that lift is not reduced during optimization;

A wing volume constraint to prevent unrealistic geometric distortion;

Airfoil thickness constraints at all wing sections to maintain structural feasibility;

Leading-edge and trailing-edge shape constraints to preserve aerodynamic smoothness;

A structural strength constraint based on the Von Mises stress, with a safety factor of 1.5, ensuring that the maximum stress remains below the allowable limit.

The aerostructural coupled optimization problem considered in this study can be written in the following standard form:

$$\text{minimize\_\{x\}} \ \backslash\text{quad C\_D(x, q\_a\^*(x), q\_s\^*(x))}$$

subject to

$$C_L(x, q_a^*(x), q_s^*(x)) \geq C_{L,\text{target}} = 0.3702,$$

$$V(x) \geq V_\text{initial},$$

$$0.5T_{\text{initial},i} \leq T_i(x) \leq 3.0T_{\text{initial},i},\ i = 1, \ldots, 450,$$

$$\Delta Y_{\text{LE},i}^{\text{up}} = \Delta Y_{\text{LE},i}^{\text{down}},\ i = 1, \ldots, 30,$$

$$\Delta Y_{\text{TE},i}^{\text{up}} = \Delta Y_{\text{TE},i}^{\text{down}},\ i = 1, \ldots, 30,$$

$$\text{KS}_\sigma(x, q_s^*(x)) \leq 0.64,$$

$$-0.015 \leq \Delta y_j \leq 0.015,\ j = 1, \ldots, 450,$$

$$-2^\circ \leq \gamma_k \leq 2^\circ,\ k = 1, \ldots, 30,$$

$$-1 \leq \Delta x_\text{eng} \leq 1,\ -0.3 \leq \Delta y_\text{eng} \leq 1,\ -1 \leq \Delta z_\text{eng} \leq 1.$$

$$R_a(q_a, q_s, x) = 0, \quad R_s(q_a, q_s, x) = 0.$$

Here,

$$x = \left[\Delta Y_1, \ldots, \Delta Y_{450}, \gamma_1, \ldots, \gamma_{30}, \Delta X_{\text{eng}}, \Delta Y_{\text{eng}}, \Delta Z_{\text{eng}}\right]^T \in R^{483}$$

Denotes the full design-variable vector, including the wing FFD shape variables, wing twist variables, and engine translation variables. The variables $q_a^*(x)$ and $q_s^*(x)$ denote the converged aerodynamic and structural states satisfying the coupled governing equations, where R_a and R_s represent the aerodynamic and structural residuals, respectively. The asymmetric bounds in the vertical direction reflect the geometric-clearance and installation constraints of the over-the-wing configuration. In addition, KS_σ denotes the Kreisselmeier–Steinhauser aggregation of the normalized Von Mises stress. Accordingly, the present problem is a PDE-constrained aerostructural optimization problem in which the objective and constraints are evaluated on the converged coupled aerodynamic–structural equilibrium state.

The structural constraint is imposed using the Kreisselmeier–Steinhauser (KS) aggregation of the normalized Von Mises stress.

Before performing the full optimization, the accuracy of the discrete adjoint gradients is verified. Four FFD control points are arbitrarily selected, and perturbations are applied in the vertical direction. The gradients of the drag coefficient C_D and lift coefficient C_L with respect to these perturbations are computed.

Three common approaches are available for gradient verification: finite difference, complex-step, and forward-mode automatic differentiation. In this study, forward-mode automatic differentiation is employed as the reference method. The verification is conducted under the same conditions as the initial aerostructural analysis.

The comparison between the gradients computed using the discrete adjoint method and those obtained using forward-mode differentiation is presented in Tables 8 and 9. In these tables, the red digits indicate discrepancies in significant figures relative to the reference values. The results show that the adjoint-based gradients of C_D match the forward-mode results to at least seven significant digits, while the gradients of C_L match to at least six significant digits. These results confirm the high accuracy of the discrete adjoint method used in the present multidisciplinary coupled framework.

Table 8. Comparison of adjoint and forward-mode derivatives of the drag coefficient C_D.

	dC_D/dFFD	
Perturbation Point	**Forward-Mode AD**	**Discrete Adjoint**
Perturbation point 1	0.0001301858500768	0.0001301858444554
Perturbation point 2	0.0007390651101238	0.0007390657258943
Perturbation point 3	−0.0001655463222576	−0.0001655354342494
Perturbation point 4	−0.0000031013008512	−0.0000031252217709

Table 9. Comparison of adjoint and forward-mode derivatives of the lift coefficient C_L.

	dC_L/dFFD	
Perturbation Point	**Forward-Mode AD**	**Discrete Adjoint**
Perturbation point 1	−0.0000057040811543	−0.0000057040804874
Perturbation point 2	−0.0000359170236209	−0.0000359170769634
Perturbation point 3	0.0000063000327204	0.0000062996166333
Perturbation point 4	0.0000000987306802	0.0000000992852811

Based on the validated adjoint framework and the optimization problem formulation, the multidisciplinary coupled adjoint optimization is performed. The optimization is carried out on the "Chang Kong II" high-performance computing system at Nanjing University of Aeronautics and Astronautics, using 4 computing nodes with a total of 192 CPU cores. The total wall-clock time for the optimization is approximately 61 h.

During the optimization, the flow solver convergence tolerance is set to 1×10^{-5}, consistent with the convergence study in Section 3.2. The maximum number of flow solver iterations per coupling cycle is 1000, and the adjoint equations are solved using the GMRES with a maximum of 1000 iterations per adjoint solve. The peak memory usage during the optimization reaches approximately 492 GB. The IPOPT optimizer is employed to solve the constrained nonlinear optimization problem.

After 308 optimization iterations, the flow residuals converge to 1×10^{-5}, and the adjoint residuals of both the lift and drag coefficients converge to 1×10^{-3}. The convergence histories of the flow solver, adjoint solver, and optimization process are shown in Figures 14–19.

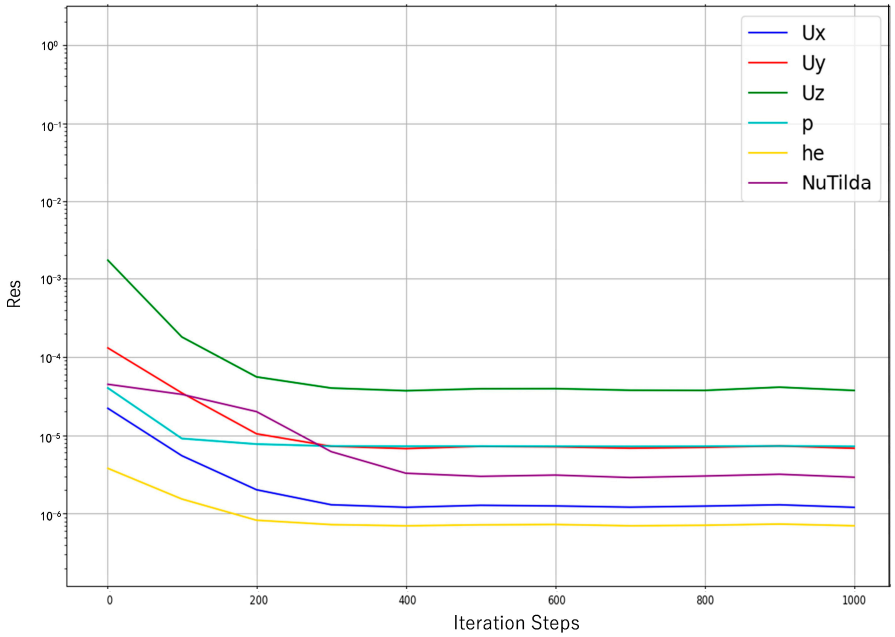

Figure 14. Convergence history of the flow solver during optimization.

The optimized results are summarized in Table 10 After optimization, the engine is translated by 0.506 m in the chordwise direction, 0.119 m in the vertical direction, and −0.186 m in the spanwise direction. With the combined effects of wing shape optimization, engine position adjustment, engine jet effects, and static aeroelastic deformation, the optimized configuration achieves a 9.51% reduction in total drag while satisfying the lift and structural stress constraints.

It should be noted that during certain intermediate optimization iterations, the lift constraint is temporarily violated. This behavior arises because IPOPT is an infeasible interior-point method [27], which allows temporary constraint violations during iterations while gradually steering the solution toward feasibility. This property enhances robustness for highly nonlinear, large-scale optimization problems and avoids stagnation issues commonly encountered in strictly feasible interior-point methods.

The convergence histories of the objective and constraint functions, as well as comparisons of pressure coefficient distributions before and after optimization, are shown in Figures 20 and 21. The results indicate that, prior to optimization, strong shock waves

exist between the engine nacelle and the wing trailing edge, which are the primary source of interference drag. After optimization, these strong shocks are effectively eliminated, resulting in a smoother pressure recovery and a significant reduction in drag.

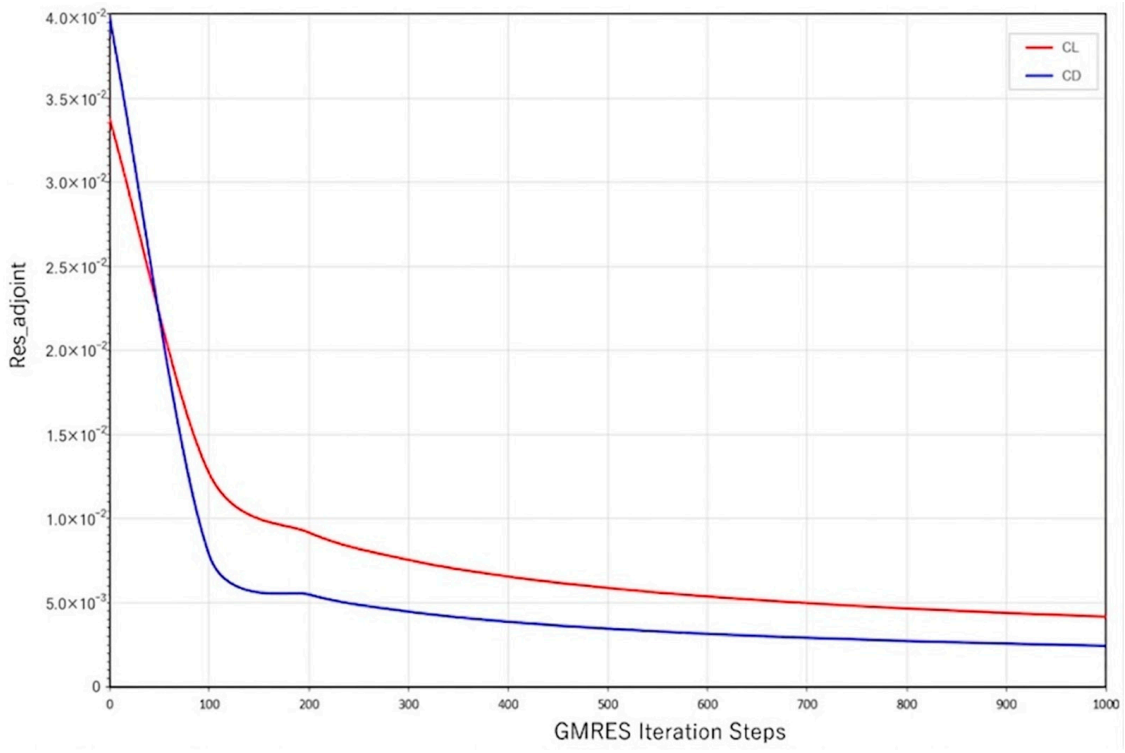

Figure 15. Convergence history of the adjoint solver during optimization.

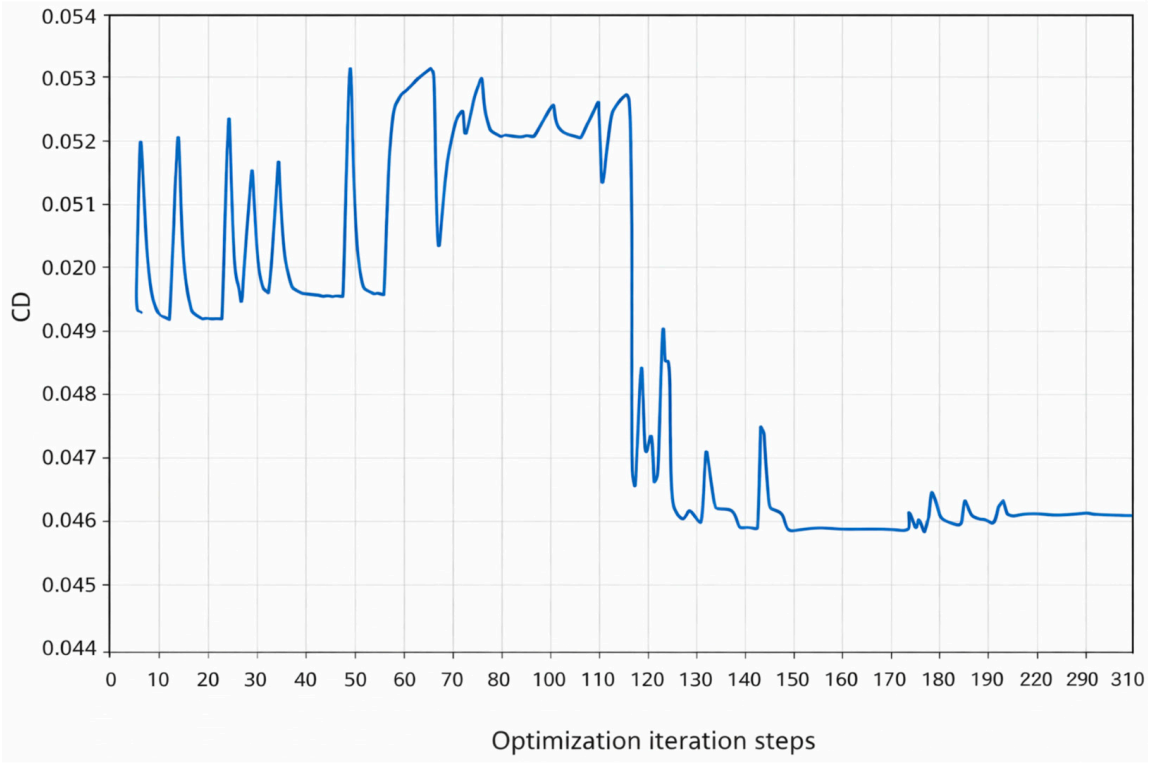

Figure 16. Convergence history of the drag coefficient C_D.

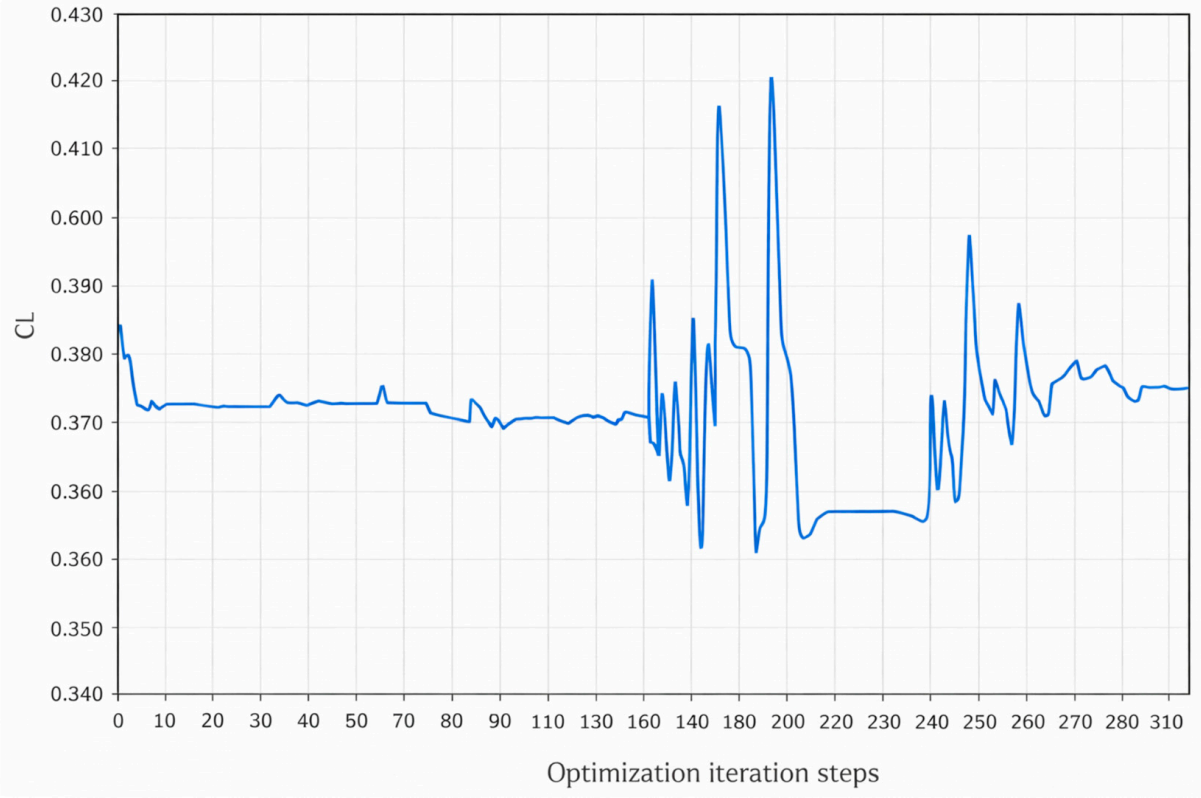

Figure 17. Convergence history of the lift coefficient C_L.

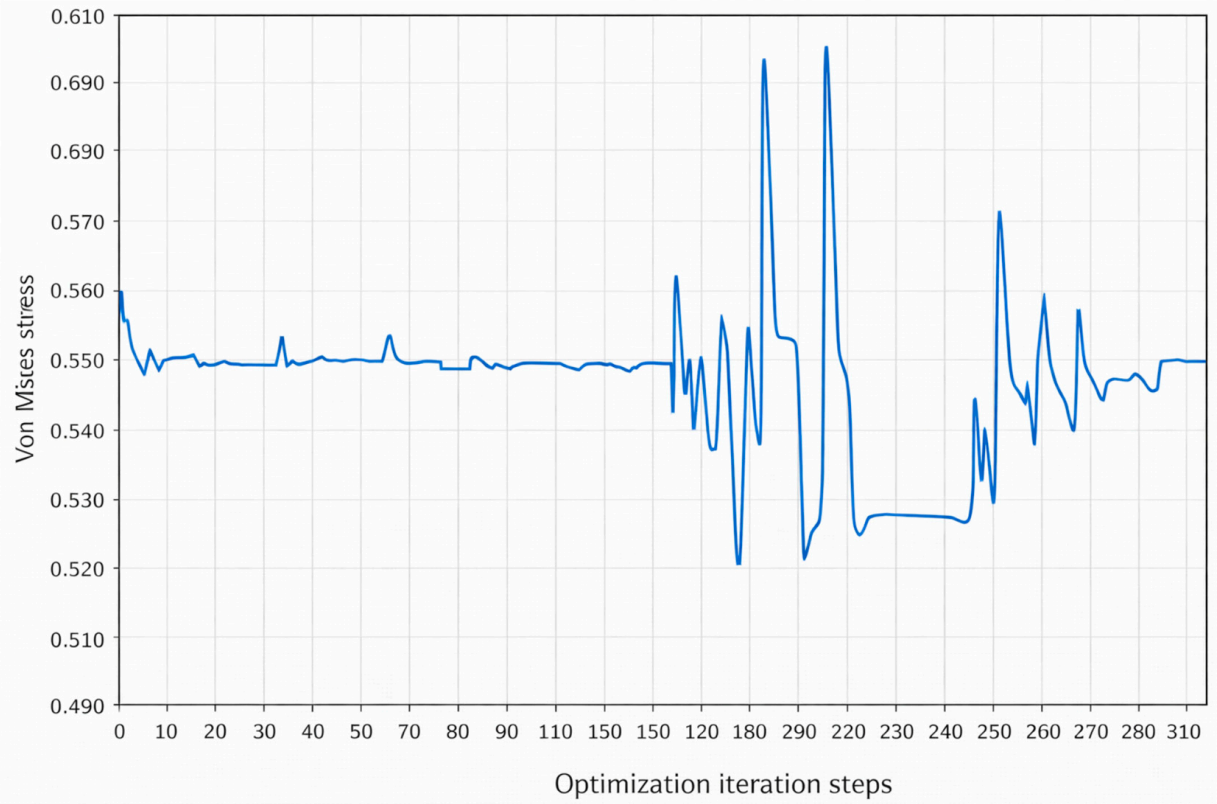

Figure 18. Convergence history of the Von Mises stress constraint.

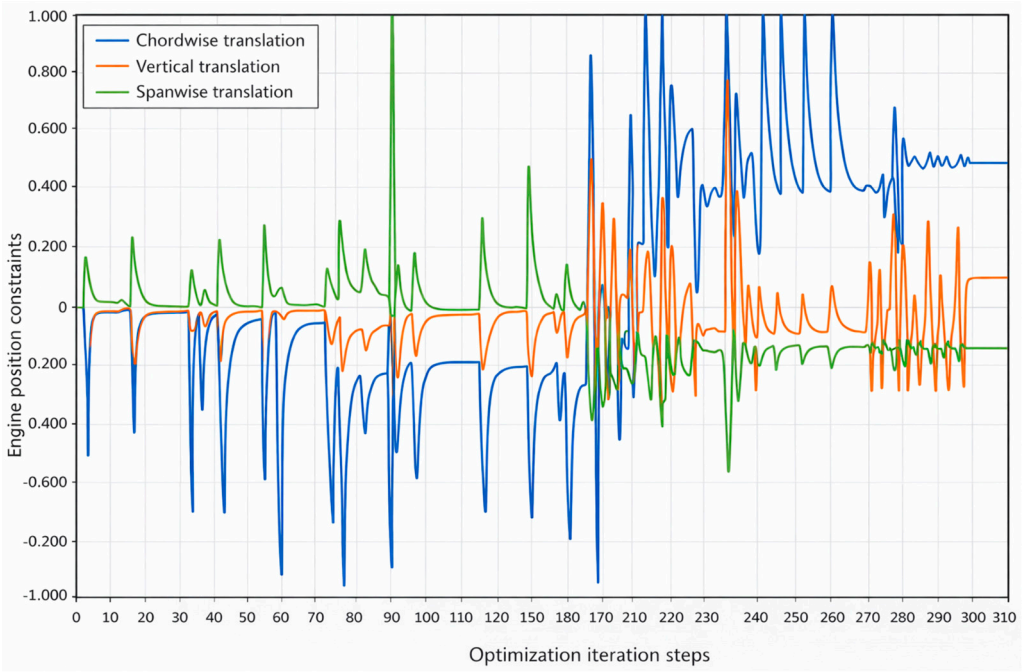

Figure 19. Convergence history of engine position in optimization.

Table 10. Comparison of aerodynamic and structural performance before and after optimization.

Category	Variable	Before Optimization	After Optimization	Change
Optimization objective	C_D	0.04554	0.04121	**−9.508%**
Lift constraint	C_L	0.3702	0.3726	**+0.648%**
Stress constraint	VM_{stress}	0.5459	0.5436	**−0.421%**

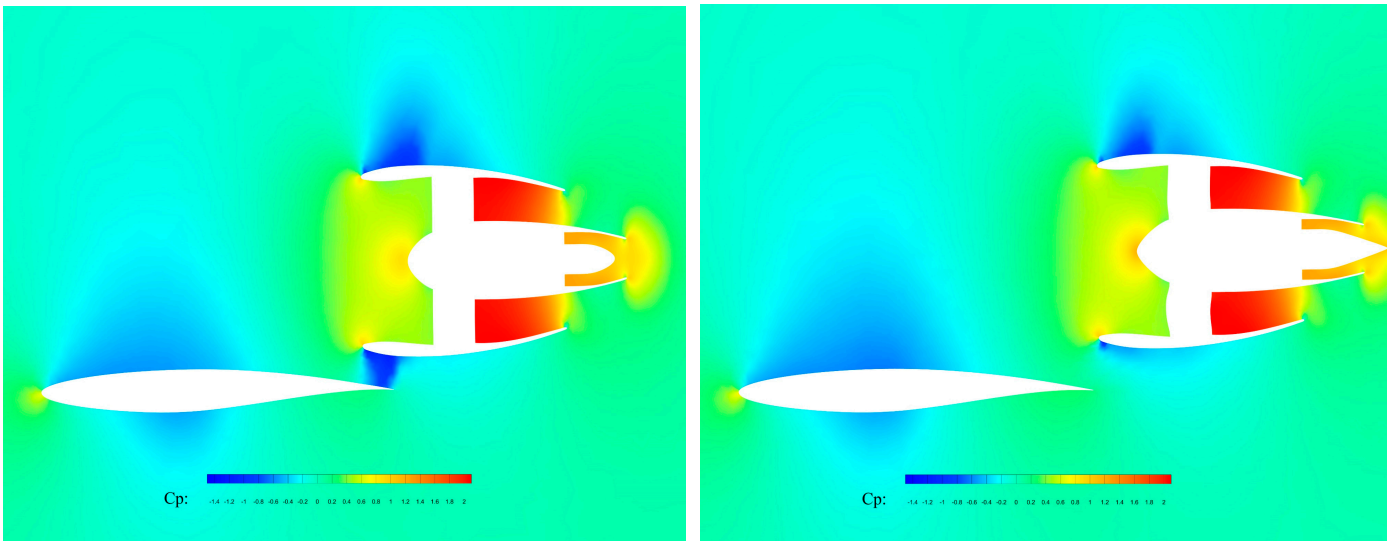

(a) Initial Aeroelastic Shape (b) Optimized Shape

Figure 20. Comparison of upper-surface pressure contours before and after optimization.

However, while shock elimination contributes to drag reduction, shock-associated acceleration regions also generate additional lift. Therefore, eliminating shocks alone would inevitably lead to lift loss. Comparisons of the wing airfoil shapes and pressure coefficient distributions at several spanwise locations before and after optimization are presented in Figures 22–26. The results demonstrate that the optimized wing shape introduces a

more favorable pressure gradient on the upper surface, which compensates for the lift loss associated with shock elimination and further improves aerodynamic performance. These results should not be interpreted as a trivial consequence of moving the nacelle rearward. Fujino and Kawamura [5] showed that wave-drag reduction can be achieved only when the nacelle front face is properly matched to the shock position on the wing and the vertical spacing is maintained within an appropriate range, rather than through nacelle translation alone. Ahuja et al. [6] further demonstrated that nacelle chordwise placement is the dominant installation parameter, but that outer-mold-line contouring is equally critical for over-the-wing nacelle performance, and that nacelle placement studies in isolation are insufficient for aerodynamically competitive OWN concepts. Consistent with these findings, the present drag reduction results from a coordinated mechanism: nacelle repositioning mainly alleviates the local nacelle–wing shock interaction, whereas wing shape and twist optimization reconstruct the upper-surface pressure gradient and compensate for the lift loss associated with shock alleviation. Therefore, the final optimum should be understood as a coupled wing–nacelle optimum rather than a position-only optimum.

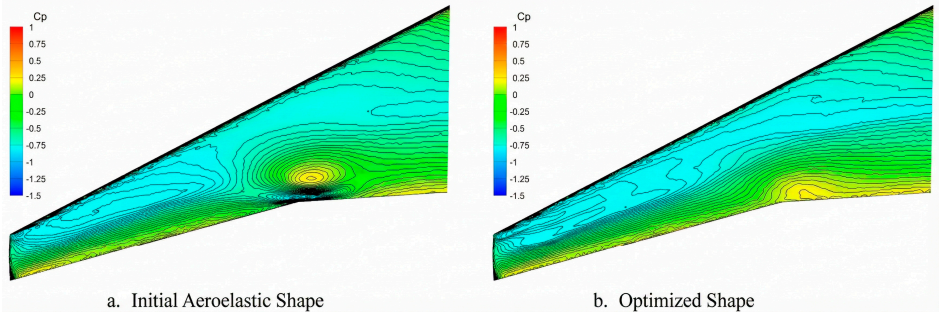

Figure 21. Comparison of wing isobar distributions before and after optimization.

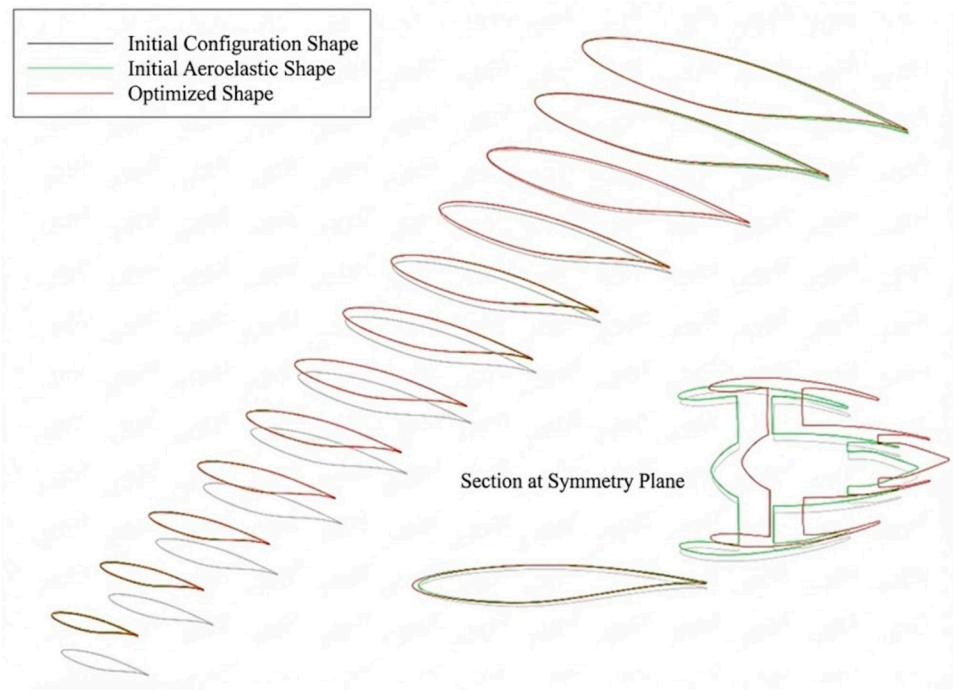

Figure 22. Comparison of overall wing airfoil profiles before and after optimization.

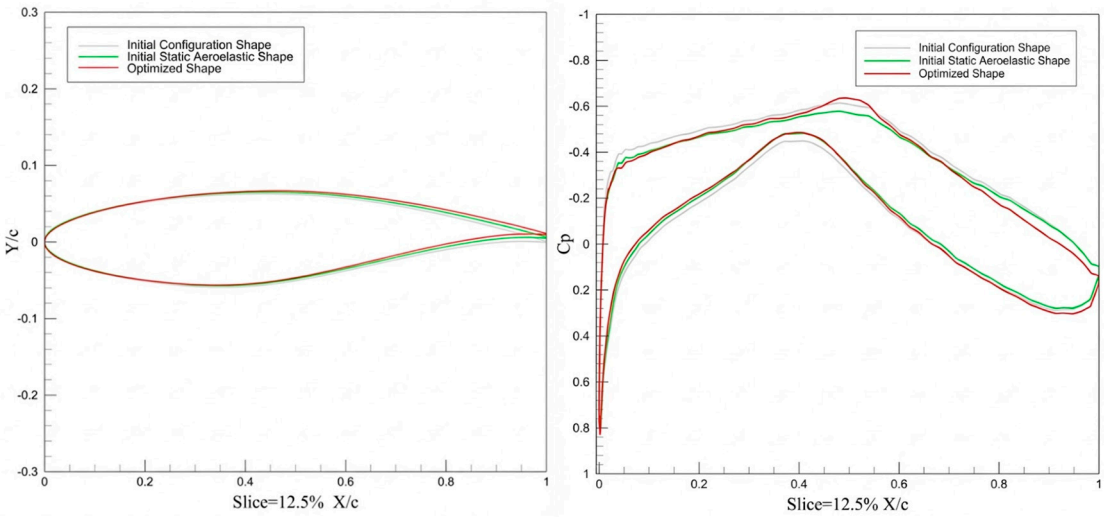

Figure 23. Comparison of the airfoil shape and pressure distribution along the span (slice = 12.5%).

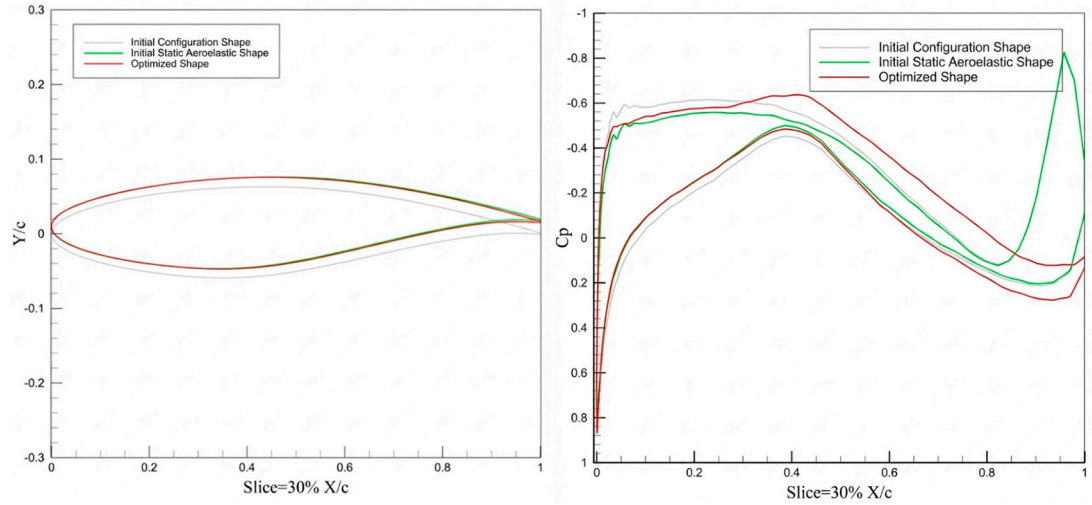

Figure 24. Comparison of the airfoil shape and pressure distribution along the span (slice = 30%).

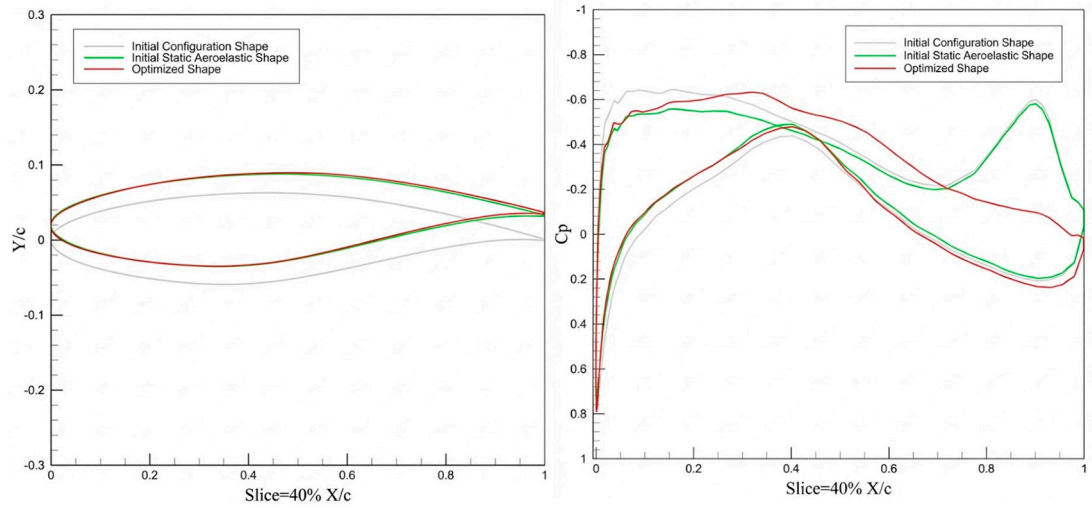

Figure 25. Comparison of the airfoil shape and pressure distribution along the span (slice = 40%).

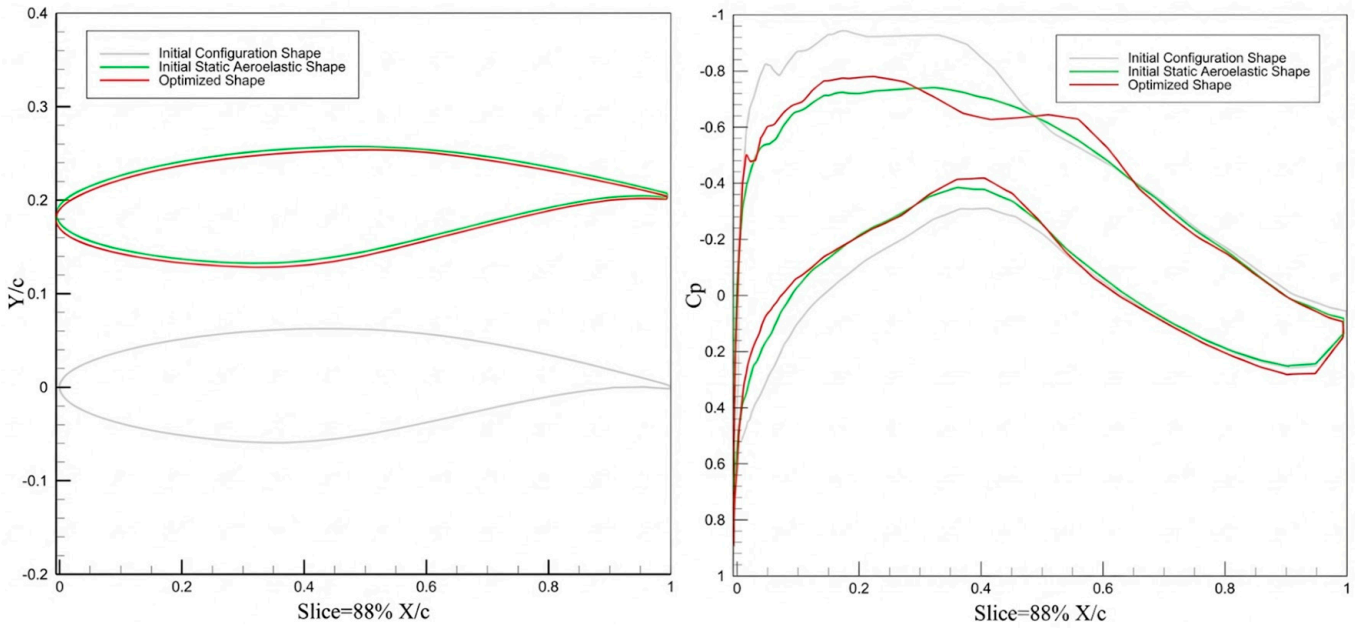

Figure 26. Comparison of the airfoil shape and pressure distribution along the span (slice = 88%).

To further interpret the optimization mechanism from a whole-wing perspective, Figure 27 compares the normalized spanwise loading distributions of the initial rigid shape, the initial aeroelastic shape, the optimized shape, and an elliptic loading reference. Relative to the initial rigid shape, the initial aeroelastic shape shows an overall reduction in loading, especially over the outboard wing, which is consistent with the unloading effect induced by static aeroelastic deformation. More importantly, relative to the initial aeroelastic shape, the optimized configuration restores the loading in the nacelle-affected inboard wing region while slightly unloading the mid- and outboard wing. As a result, the overall loading distribution becomes smoother and shows a trend closer to the elliptic reference. This indicates that the drag reduction should not be interpreted as a trivial consequence of aft nacelle translation alone. Instead, nacelle repositioning mainly alleviates the local nacelle–wing shock interaction, whereas wing shape and twist modifications redistribute the spanwise loading to compensate for the lift loss associated with shock alleviation and to reduce the penalty associated with nonuniform wing loading. Therefore, the final optimum should be understood as a coupled wing–nacelle optimum rather than a position-only optimum.

It should be noted that the pronounced local variation near the nacelle spanwise station reflects aerodynamic load redistribution of the integrated wing–nacelle configuration caused by nacelle repositioning, nacelle–wing interference, and the prescribed engine inlet/exhaust effects, rather than the direct effect of engine concentrated mass or gravity/inertial loads.

From a structural perspective, comparisons of spanwise structural displacement and Von Mises stress distributions before and after optimization are shown in Figures 28 and 29. The results indicate that the structural displacement distributions remain largely unchanged, and the maximum structural stress does not increase after optimization, confirming that the optimized configuration satisfies the imposed structural constraints.

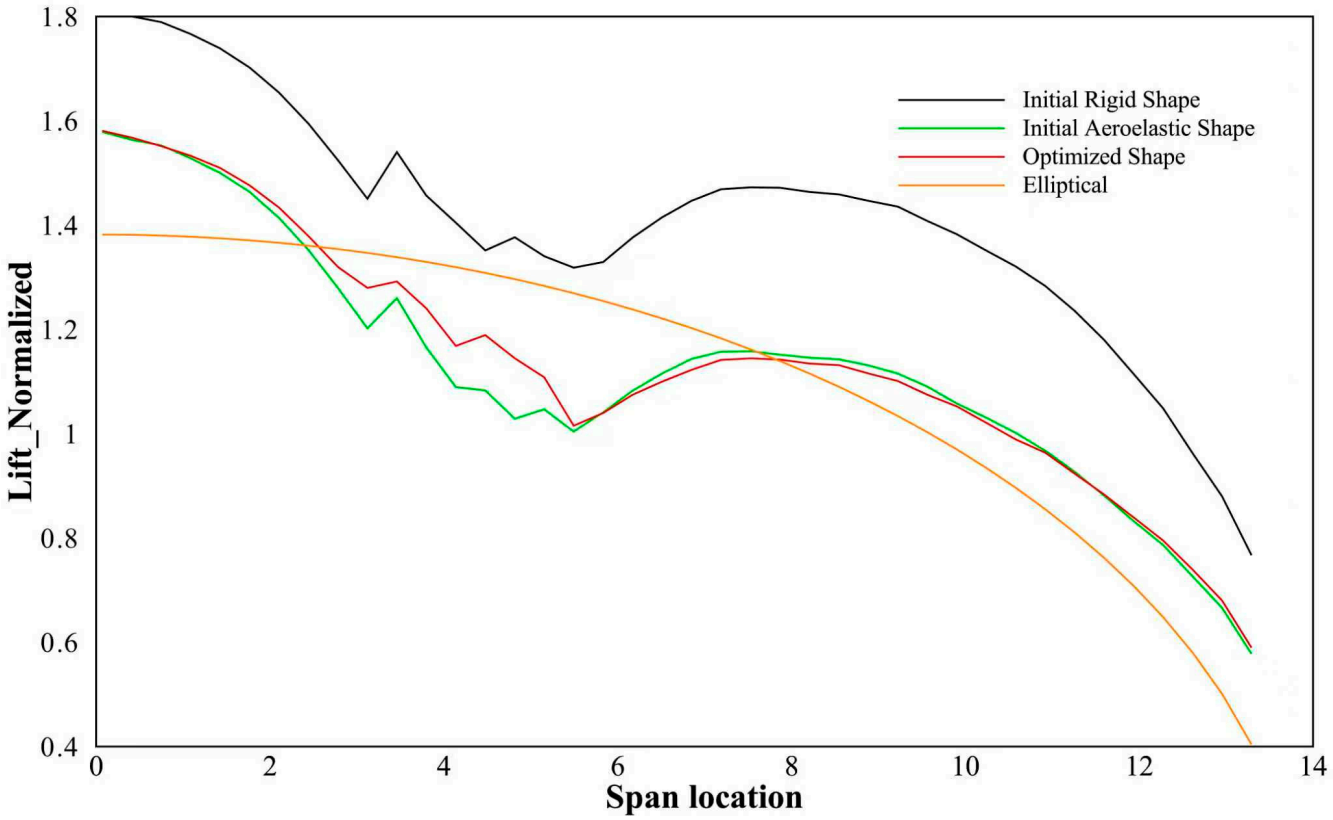

Figure 27. Comparison of normalized spanwise loading distributions.

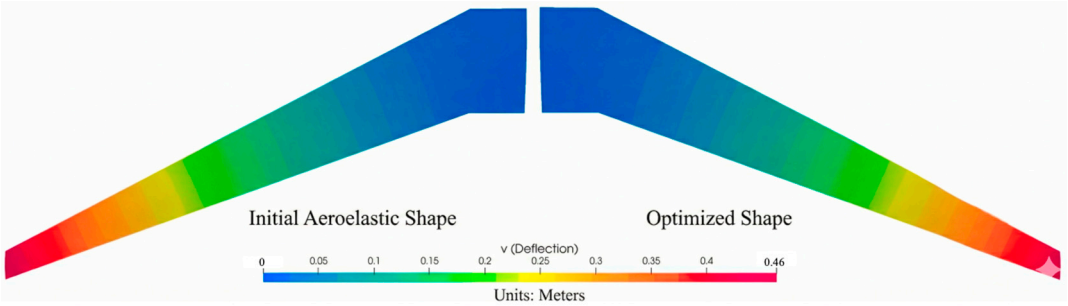

Figure 28. Comparison of wingbox structural displacement along the span.

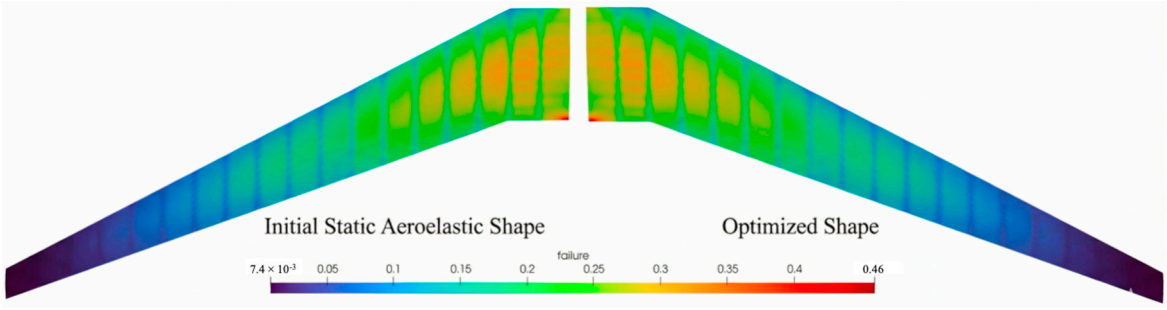

Figure 29. Comparison of wingbox structural stress along the span.

4. Conclusions

This study addresses the key technical challenges associated with over-the-wing engine mount configurations by developing a comprehensive multidisciplinary coupled analysis and discrete adjoint-based drag reduction optimization framework based on the open-source OpenMDAO platform. A complete workflow is established, covering theoretical for-

mulation, framework implementation, and engineering application, thereby demonstrating a practical adjoint-based optimization pathway for over-the-wing engine configurations.

Through the optimization of a representative over-the-wing engine configuration, the proposed framework achieves a 9.51% reduction in cruise drag while satisfying the prescribed lift constraint and structural stress constraints. These results verify the effectiveness of the developed multidisciplinary coupled adjoint optimization framework and further confirm the aerodynamic potential of over-the-wing engine mount configurations.

The results reveal strong interactions between wing geometry and engine nacelle installation position for over-the-wing engine configurations. Previous OWN studies have shown that favorable aerodynamic interference depends on matching the nacelle position to the wing shock system and that nacelle placement studies in isolation are not sufficient for aerodynamically competitive OWN concepts. Consistent with these findings, the present results indicate that coordinated optimization of both wing aerodynamic shape and engine installation parameters is essential. Adjusting the engine position mainly alleviates the local nacelle–wing shock interaction, whereas the simultaneous modification of wing geometry is required to reconstruct the upper-surface pressure distribution, compensate for the lift loss associated with shock weakening, and fully realize the aerodynamic benefits of the configuration.

Flow visualization results indicate that the interaction between the flow field induced by the engine nacelle and the wing external flow has a significant influence on overall wing performance. Effective design optimization for over-the-wing engine configurations must balance two key aspects. First, strong shock waves generated by the interaction between the wing and the engine nacelle should be eliminated or weakened through appropriate optimization of wing shape and engine position. Second, the wing geometry and engine installation must be matched to improve the pressure distribution on the upper surface of the wing, thereby generating a stronger favorable pressure gradient that compensates for the lift loss associated with shock elimination and further improves drag characteristics. This mechanism, often referred to as favorable interference, is fundamental to achieving simultaneous drag reduction and lift preservation for over-the-wing engine configurations.

Overall, the present study demonstrates that adjoint-based multidisciplinary coupled optimization provides an effective and scalable approach for the design of over-the-wing engine mount configurations.

It should also be emphasized that the present structural analysis is based on a simplified wingbox static aeroelastic model and does not explicitly include engine concentrated mass, pylon stiffness, gravity/inertial loads, or the detailed structural load redistribution induced by engine-position changes. Therefore, the conclusions of this study are mainly limited to the aerodynamic–static-aeroelastic drag-reduction mechanism of the over-the-wing configuration at the cruise design point, and should not be directly interpreted as final engineering conclusions regarding engine-placement feasibility in terms of detailed structural design, flutter characteristics, or pylon design.

The developed framework offers a solid foundation for future investigations involving higher-fidelity propulsion models, dynamic aeroelastic effects, and more complex aircraft configurations. Furthermore, the current MDO framework assumes a fixed engine performance at the cruise design point. If engine performance parameters, such as thrust or mass flow rate, were to vary dynamically, the jet-induced interference and structural load distribution would shift accordingly. Future work will investigate the sensitivity of the optimal aerostructural shape to variable engine operating conditions.

Author Contributions: Conceptualization, C.Y. and Y.G.; methodology, C.Y., A.Z. and Y.G.; software, C.Y. and A.Z.; validation, C.Y., A.Z. and F.Q.; formal analysis, C.Y.; investigation, C.Y. and A.Z.; resources, X.C. and Y.G.; data curation, C.Y.; writing—original draft preparation, C.Y.; writing—

review and editing, F.Q., X.C. and Y.G.; visualization, C.Y. and A.Z.; supervision, Y.G.; project administration, Y.G.; funding acquisition, Y.G. All authors have read and agreed to the published version of the manuscript.

Funding: This research received no external funding.

Institutional Review Board Statement: Not applicable.

Informed Consent Statement: Not applicable.

Data Availability Statement: The data supporting the findings of this study are available from the corresponding author upon reasonable request.

Acknowledgments: Grateful acknowledgment is made to He Ping for valuable technical discussions and constructive suggestions related to the DAFoam solver and adjoint-based optimization methodology. Appreciation is also extended to the DAFoam community and its GitHub forum for providing an open and active platform that significantly supported the development, debugging, and validation of the computational framework used in this study. Computational resources provided by the High-Performance Computing Center of Nanjing University of Aeronautics and Astronautics are also gratefully acknowledged.

Conflicts of Interest: The authors declare no conflict of interest.

References

1. Kellari, D.; Crawley, E.F.; Cameron, B.G. Influence of technology trends on future aircraft architecture. *J. Aircr.* **2017**, *54*, 2213–2227. [CrossRef]
2. Berguin, S.; Mavris, D. Interactions in over-wing nacelle optimization. In Proceedings of the 51st AIAA Aerospace Sciences Meeting Including the New Horizons Forum and Aerospace Exposition, Grapevine, TX, USA, 7–10 January 2013.
3. Abdul-Kaiyoom, M.A.S.; Yildirim, A.; Martins, J.R.R.A. RANS-based multipoint aeropropulsive design optimization of an over-wing nacelle configuration. In Proceedings of the AIAA Aviation Forum, San Diego, CA, USA, 12–16 June 2023.
4. Lange, F.; Rudnik, R. Numerical position optimization of an over-the-wing mounted engine installation. *CEAS Aeronaut. J.* **2021**, *12*, 135–146. [CrossRef]
5. Fujino, M.; Kawamura, Y. Wave-drag characteristics of an over-the-wing nacelle business-jet configuration. *J. Aircr.* **2003**, *40*, 1177–1184. [CrossRef]
6. Ahuja, J.; Renganathan, S.A.; Mavris, D.N. Sensitivity analysis of the overwing nacelle design space. *J. Aircr.* **2022**, *59*, 1478–1492. [CrossRef]
7. Fujino, M. Design and development of the HondaJet. *J. Aircr.* **2005**, *42*, 755–764. [CrossRef]
8. Mader, C.A.; Kenway, G.K.W.; Yildirim, A.; Martins, J.R.R.A. ADflow: An open-source computational fluid dynamics solver for aerodynamic and multidisciplinary optimization. *J. Aerosp. Inf. Syst.* **2020**, *17*, 508–527. [CrossRef]
9. Kennedy, G.J.; Martins, J.R.R.A. A parallel finite-element framework for large-scale gradient-based design optimization of high-performance structures. *Finite Elem. Anal. Des.* **2014**, *87*, 56–73. [CrossRef]
10. Martins, J.R.R.A. Perspectives on aerodynamic design optimization. In Proceedings of the AIAA SciTech Forum, Orlando, FL, USA, 6–10 January 2020.
11. Gray, J.S.; Hwang, J.T.; Martins, J.R.R.A.; Moore, K.T.; Naylor, B.A. OpenMDAO: An open-source framework for multidisciplinary design, analysis, and optimization. *Struct. Multidiscip. Optim.* **2019**, *59*, 1075–1104. [CrossRef]
12. He, P.; Mader, C.A.; Martins, J.R.R.A.; Maki, K.J. DAFoam: An open-source adjoint framework for multidisciplinary design optimization with OpenFOAM. *AIAA J.* **2020**, *58*, 1304–1319. [CrossRef]
13. Jasak, H. OpenFOAM: Open source CFD in research and industry. *Int. J. Nav. Archit. Ocean Eng.* **2009**, *1*, 89–94.
14. Hendricks, E.S.; Gray, J.S. pyCycle: A tool for efficient optimization of gas turbine engine cycles. *Aerospace* **2019**, *6*, 87. [CrossRef]
15. Lytle, J.; Follen, G.; Naiman, C.; Evans, A. *Numerical Propulsion System Simulation (NPSS) 1999 Industry Review*; NASA/TM-2000-209795; NASA Glenn Research Center: Cleveland, OH, USA, 2000.
16. Yildirim, A.; Gray, J.S.; Mader, C.A.; Martins, J.R.R.A. Aeropropulsive design optimization of a boundary layer ingestion system. In Proceedings of the AIAA Aviation Forum, Dallas, TX, USA, 17–21 June 2019.
17. Van Doormaal, J.P.; Raithby, G.D. Enhancements of the SIMPLE method for predicting incompressible fluid flows. *Numer. Heat Transf.* **1984**, *7*, 147–163. [CrossRef]
18. Spalart, P.R.; Allmaras, S.R. A one-equation turbulence model for aerodynamic flows. In Proceedings of the 30th Aerospace Sciences Meeting and Exhibit, Reno, NV, USA, 6–9 January 1992.

19. Kennedy, G.J.; Martins, J.R.R.A. A parallel aerostructural optimization framework for aircraft design studies. *Struct. Multidiscip. Optim.* **2014**, *50*, 1079–1101. [CrossRef]
20. Yildirim, A.; Jacobson, K.E.; Anibal, J.L.; Stanford, B.K.; Gray, J.S.; Mader, C.A.; Martins, J.R.R.A.; Kennedy, G.J. MPhys: A modular multiphysics library for coupled simulation and adjoint derivative computation. *Struct. Multidiscip. Optim.* **2025**, *68*, 15. [CrossRef]
21. Blazek, J. *Computational Fluid Dynamics: Principles and Applications*; Butterworth-Heinemann: Oxford, UK, 2015.
22. Kenway, G.K.; Mader, C.A.; He, P.; Martins, J.R. Effective adjoint approaches for computational fluid dynamics. *Prog. Aerosp. Sci.* **2019**, *110*, 100542. [CrossRef]
23. Heykena, C.; Savoni, L.; Friedrichs, J.; Rudnik, R. Engine airframe integration sensitivities for a STOL commercial aircraft concept with over-the-wing mounted UHBR-turbofans. In Proceedings of the Global Power and Propulsion Forum, Montreal, QC, Canada, 7–9 May 2018.
24. Brooks, T.R.; Kenway, G.K.W.; Martins, J.R.R.A. Benchmark aerostructural models for the study of transonic aircraft wings. *AIAA J.* **2018**, *56*, 2840–2855. [CrossRef]
25. Hajdik, H.M.; Yildirim, A.; Wu, E.; Brelje, B.J.; Seraj, S.; Mangano, M.; Anibal, J.L.; Jonsson, E.; Adler, E.J.; Mader, C.A.; et al. pyGeo: A geometry package for multidisciplinary design optimization. *J. Open Source Softw.* **2023**, *8*, 5319. [CrossRef]
26. Secco, N.R.; Kenway, G.K.W.; He, P.; Mader, C.; Martins, J.R.R.A. Efficient mesh generation and deformation for aerodynamic shape optimization. *AIAA J.* **2021**, *59*, 1151–1168. [CrossRef]
27. Biegler, L.T.; Zavala, V.M. Large-scale nonlinear programming using IPOPT: An integrating framework for enterprise-wide dynamic optimization. *Comput. Chem. Eng.* **2009**, *33*, 575–582. [CrossRef]